Sajeeva Abeywardena[1]
School of Electronic Engineering and Computer Science
Queen Mary University of London, UK
email: s.abeywardena@qmul.ac.uk

Eisa Anwar
School of Electronic Engineering and Computer Science
Queen Mary University of London, UK
email: e.a.m.anwar@qmul.ac.uk

Stuart Charles Miller
William Harvey Research Institute
Barts & The London School of Medicine & Dentistry
Queen Mary University of London, UK
email: stuart.miller@qmul.ac.uk

Ildar Farkhatdinov[1]
School of Engineering and Material Science
Queen Mary University of London, UK
Department of Bioengineering
Imperial College of Science, Technology and Medicine, London, UK
email: i.farkhatdinov@qmul.ac.uk

Mechanical characterisation of supernumerary robotic tails for human balance augmentation

Humans are intrinsically unstable in quiet stance from a rigid body system viewpoint; however, they maintain balance thanks to neuro-muscular sensory control properties. With increasing levels of balance related incidents in industrial and ageing populations globally each year, the development of assistive mechanisms to augment human balance is paramount. This work investigates the mechanical characteristics of kinematically dissimilar one and two degrees-of-freedom supernumerary robotic tails for balance augmentation. Through dynamic simulations and manipulability assessments, the importance of variable coupling inertia in creating a sufficient reaction torque is highlighted. It is shown that two-dof tails with solely revolute joints are best suited to address the balance augmentation issue. Within the two-dof options, the characteristics of open versus closed loop tails is investigated, with the ultimate design selection requiring trade-offs between environmental workspace, biomechanical factors and manufacturing ease to be made.

Keywords: Supernumerary Robotic Limbs; Human Balance; Dynamics; Wearable Robotics; Human Performance Augmentation; Physical Human-Robot Interaction

1 Introduction

Fall related incidents are a leading cause of accidental injury and fatalities, with over 684 000 fall related deaths and a further 172 million falls that result in either short or long term disability a year [1]. Those at greatest risk of suffering such incidents are industrial workers and the ageing population. In recent years, the utilisation of wearable assistive devices to augment human balance have been researched; with occupational back support exoskeletons for workplace intervention [2,3] and lower limb exoskeletons for the general population [4–6] having promising results. Due to being attached in parallel with the natural limbs of the wearer; exoskeletons share the same kinematic properties as the assisted limb but the added mass and footprint of the wearable device can hinder the natural motion capabilities of the limbs.

Supernumerary robotic limbs attach to the human body and work with the natural limbs to extend the kinematic workspace. Hence, they have key characteristics to facilitate augmentation of human balance. Previous works of supernumerary limbs for balance assistance have focussed on extra robotic legs to increase the base of support (BoS) during walking gait [7–9], increasing comfort and posture in near-ground work [10], and for bracing in assembly and overhead tasks to increase the support polygon and reduce muscular loads [11,12]. Increasing the BoS improves the stability of balance as force is distributed through the ground via more contact points. However, this comes at the cost of increasing the overall footprint of the human which could be an issue due to environmental workspace constraints.

Control moment gyroscopic (CMG) assist systems and supernumerary robotic tails (SRTs) provide human balance assistance without augmenting the BoS. In CMG systems, the principal of precession is utilised to counteract the torque caused by postural sway [13,14]. Supernumerary tails take inspiration from nature where animals use them for motion and balance augmentation; with a seahorse inspired pneumatically actuated tail [15] and a one-degree-of-freedom (dof) swinging rigid link tail in the coronal plane [16] being the current state of the art. Further, research has been conducted into the use of robotic tails to improve manoeuvrability of mobile robots [17–19]. However, these results are not directly transferable to augment human balance as mobile robots have a larger BoS and different mass specification such as weight and a lower CoM. For instance, the mobile robot considered in [17] is 0.177 kg, significantly less than that of an average human. Importantly, the problem of balance augmentation of humans is more complex as design and control of a supernumerary tail needs to complement the biology of the human body. This is very different from the mobile robots cited above where the design and control of robotic tails' were considered from initial development and naturally belong to the mobile robot. Hence, the domain of supernumerary tails is still in its infancy, with their ideal kinematic structure remaining an open question worthy of a thorough systematic investigation. Therefore, the novelty of this work is to explore how different kinematic configurations effect balancing capabilities which will help facilitate the mechanical design and control of a supernumerary robotic tail for human balance augmentation. This analysis of possible kinematic configurations for supernumerary robotic tails has not been conducted in previous works.

Our recent work, investigated the ability of a one-dof revolute robotic tail to augment quiet standing balance [20]. In this work, the kinematic and dynamic characteristics of a series of one and two-dof robotic tails, and their suitability to augment human balance against gravitational instability is examined. This investigation utilises fundamental techniques of rigid body dynamics and control theory. As such, this is the first fundamental study to conclusively investigate and understand the ideal kinematic configuration of wearable robotic tails for human use. It is organised as follows; the necessary theoretical framework is presented in Section 2. An investigation into one-dof tails is conducted in Section 3 followed by two-dof tails in Section 4, with the major outcomes and future avenues of research in the field of supernumerary robotic

[1]Corresponding Author.
Version 1.20, July 24, 2023

tails highlighted in Section 5.

2 System Modelling and Control

Balance of humans requires the synergistic control of mechanical limbs with sensory inputs from vestibular, visual and somatic systems. Quiet standing analysis has shown that a human in an upright pose can be modelled as an inherently unstable single inverted pendulum (SIP) [21–23]. Due to the musculoskeletal and sensorimotor systems, the toppling torque induced by the gravitational force is negated and balance is maintained so long as the centre-of-mass (CoM) is within the BoS. As such, the SIP model of quiet standing is used in this work whereby a human with hands by the side is represented as one rigid body, with one-dof at the ankle joint in the sagittal plane.

The centre-of-mass of a human in a completely balanced position is located in the axis which gravity acts but opposing direction. Hence, a human will theoretically remain balanced against gravity unless perturbed by an external disturbance. If the arms are placed in front of the torso holding a load of mass m_l, the CoM of the system (human and load)—denoted as m_s in Fig. 1—is displaced slightly forward leading to potential gravitational instability. Hence, suitable control action is required by the human to prevent loss of balance. As the duration of quiet standing grows, muscle fatigue and delay due to mental tiredness will increase irrespective of physical ability, hindering maintaining upright posture. It is hypothesised that a balancing tail can assist in compensating for the unstable dynamics in the quiet standing model. The remainder of this section models a human and summarises the theoretical frameworks paramount to this investigation.

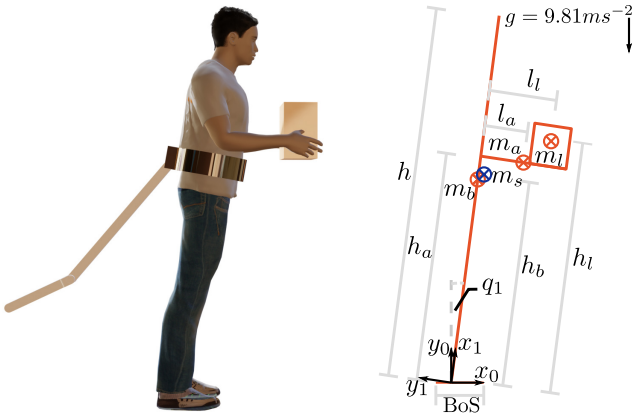

Fig. 1 A supernumerary tail aims to prevent a user from falling when their CoM exceeds the BoS. The parameter assignment of the human is shown on the right with the CoM of segments indicated as ⊗

2.1 Human Parameters .

Due to the assumption of the SIP model of stance in an upright pose, it is suffice to consider the body (legs, trunk, head), forearm and load denoted as m_b, m_a and m_l respectively in Fig. 1 as one rigid body. Hence, the CoM of the composite rigid body system can be found in the global base frame $\mathcal{F}_0$, shown as m_s in Fig. 1. A moving frame $\mathcal{F}_1$ is attached to the ankle joint to represent the rotation of the human body by angle q_1. As such, the general transformation between frames is

$$ {}^{i}\mathbf{T}_{i+1} = \begin{bmatrix} \mathbf{Q}_z\,(q_{i+1}) & {}^{i}\mathbf{p}_{i+1}\,(q_{i+1}) \\ \mathbf{0} & 1 \end{bmatrix} \tag{1} $$

$$ {}^{0}\mathbf{T}_{n} = {}^{0}\mathbf{T}_{1}\,{}^{1}\mathbf{T}_{2}\ldots{}^{n-1}\mathbf{T}_{n} \tag{2} $$

where $\mathbf{Q}_z$ is the rotation matrix about the z-axis, ${}^{i}\mathbf{p}_{i+1}$ the vector between the origins of $\mathcal{F}_i$ and $\mathcal{F}_{i+1}$ in $\mathcal{F}_i$ which are functions of q_i, the i-th generalised joint co-ordinate.

The geometric and mass parameters[2] related to Fig. 1 are tabulated in Table 1 with the inertia of the human in the sagittal plane being 12.9 kg-m^2 [24].

Table 1 The parameters with respect to Fig. 1. Distances have units of metres and mass in kilograms.

Segment (i)	h_i	l_i	m_i
Body (b)	0.997	$h = 1.8$	78.2
Arm (a)	1.11	0.225	4
Load (l)	1.23	0.354	5

2.2 Dynamic Model .

The dynamical equation of a rigid body system in terms of the motion variables can be expressed as

$$ \ddot{\mathbf{q}} = \mathbf{M}_q\,(\mathbf{q})^{-1}\left(-\mathbf{C}_q\,(\mathbf{q},\dot{\mathbf{q}})\,\dot{\mathbf{q}} - \mathbf{G}_q\,(\mathbf{q}) + \mathbf{S}\mathbf{u} + \mathbf{u}_p\right) \tag{3} $$

where $\mathbf{q}$ are the generalised joint coordinates, $\mathbf{M}_q\,(\mathbf{q})$ is the $n \times n$ generalised inertia matrix, $\mathbf{C}_q\,(\mathbf{q},\dot{\mathbf{q}})$ is an $n \times n$ matrix related to the centripetal/Coriolis torques, $\mathbf{G}_q\,(\mathbf{q})$ the vector of gravity forces, $\mathbf{u}$ and $\mathbf{u}_p$ are generalised active and passive forces and $\mathbf{S}$ is an $n \times n$ diagonal matrix that selects whether the joint is an active (1) or passive (0) input. These matrices can be found from an inverse dynamic modelling method such as Newton-Euler, Lagrangian or Natural Orthogonal Complement [25,26].

Defining the state vector $\mathbf{x} = \left[\mathbf{q}^T, \dot{\mathbf{q}}^T\right]^T$, Eq. (3) can be transformed into a system of first order ordinary differential equations (ODEs) i.e.

$$ \dot{\mathbf{x}} = \begin{bmatrix} \dot{\mathbf{q}} \\ -\mathbf{M}_q{}^{-1}\left(\mathbf{C}_q\dot{\mathbf{q}} + \mathbf{G}_q\right) \end{bmatrix} + \begin{bmatrix} \mathbf{0} \\ \mathbf{M}_q{}^{-1}\mathbf{S} \end{bmatrix}\mathbf{u} + \begin{bmatrix} \mathbf{0} \\ \mathbf{M}_q{}^{-1} \end{bmatrix}\mathbf{u}_p \tag{4} $$

From Eq. (4), it is evident that the generalised inertia matrix $\mathbf{M}_q$ is critical in the open loop response of the system, and how the control input $\mathbf{u}$ is transformed to impact the response. As such, the structure and inertial properties of a tail are significant in how it augments human balance.

As the system dynamics are non-linear, control design can be complex. Linearisation about a operating region represented as a stationary point $(\bar{\mathbf{x}}, \bar{\mathbf{u}})$ allows for concepts of linear time invariant (LTI) systems to be applied. For human balance, the operational point of interest is the upright posture. Linearising Eq. (4), the linearised state model can be derived as

$$ \dot{\mathbf{x}} = \mathbf{A}\mathbf{x} + \mathbf{B}\mathbf{u} \tag{5a} $$

$$ \mathbf{A} = \left[\begin{matrix} \mathbf{0} & \mathbf{1} \\ -\mathbf{M}_q{}^{-1}\left(\frac{\partial \mathbf{G}_q}{\partial \mathbf{q}} + \frac{\partial \mathbf{u}_p}{\partial \mathbf{q}}\right) & -\mathbf{M}_q{}^{-1}\left(\mathbf{C}_q + \frac{\partial \mathbf{u}_p}{\partial \dot{\mathbf{q}}}\right) \end{matrix}\right]\Bigg|_{\substack{\mathbf{x}=\bar{\mathbf{x}} \\ \mathbf{u}=\bar{\mathbf{u}}}} \tag{5b} $$

$$ \mathbf{B} = \left[\begin{matrix} \mathbf{0} \\ \mathbf{M}_q{}^{-1}\mathbf{S} \end{matrix}\right]\Bigg|_{\substack{\mathbf{x}=\bar{\mathbf{x}} \\ \mathbf{u}=\bar{\mathbf{u}}}} \tag{5c} $$

with $\mathbf{A}$ a $n \times n$ matrix and $\mathbf{B}$ a $n \times m$ matrix; n representing the number of states, m the number of control inputs. The eigenvalues of the state matrix $\mathbf{A}$ represent the open-loop poles of the system and indicate the inherent stability of the system. If $\mathbf{u}$ is null, the dynamics governed by Eq. (5) will drive a stable system to the state vector $\mathbf{x} = \mathbf{0}$, i.e. zero change around the stationary point $\bar{\mathbf{x}}$. For an unstable set of open loop poles, the states $\mathbf{x} \to \infty$ and the use of control action $\mathbf{u}$ is required to stabilise the system (if it is controllable). Using LTI theory, full state feedback controllers of the form $\mathbf{u} = \mathbf{K}\mathbf{x}$ can be developed to regulate the dynamics of the system to the stationary point, where $\mathbf{K}$ is a gain matrix. This is sufficient to analyse the characteristics of kinematically dissimilar SRTs to augment human balance.

[2]Note, for the arm, l_a is reported as half the total length of the segments and the mass corresponds to two arms.

2.3 Human Control . The mechanical stiffness of a human ankle is less than the critical stiffness required to negate gravitational torque. As such, balance is maintained with assistance of a neural control element that has an associated time delay [21,23]. These properties can be modelled as passive inputs $\mathbf{u}_p$ in terms of the states of the system i.e.

$$\mathbf{u}_p = \mathbf{u}_{ank} + \mathbf{u}_{nm} \tag{6}$$

$$\mathbf{u}_{ank} = \kappa_p \left(\bar{q}_1 - q_1\right) + \kappa_d \left(\dot{\bar{q}}_1 - \dot{q}_1\right)$$

$$\mathbf{u}_{nm} = k_p \left(\bar{q}_1 - q_1 \left(t - \tau_d\right)\right) + k_d \left(\dot{\bar{q}}_1 - \dot{q}_1 \left(t - \tau_d\right)\right)$$

where $\mathbf{u}_{ank}$ is a stiffness model of the ankle joint and $\mathbf{u}_{nm}$ is the neural control input with time delay τ_d.

Due to the saddle-type instability associated with upright stance; intermittent control paradigms have been proposed to explain neuromechanical control in quiet standing [23,27]. The time delay converts the ODE of Eq. (5) to a delay differential equation with infinite poles. As $\tau_d \to \infty$, the $\mathbf{u}_{nm}$ term becomes insignificant in control. This is symbolic of increasing strain on the neuro-controller due to mental tiredness, inherent motor control disorders or potential momentary loss of vestibular or somatic function, i.e. situations where a balancing robotic tail is of increased value. As this investigation is a fundamental insight into the mechanical characterisation of SRTs and not their optimal control, the worst case scenario of large neuromechanical delay is considered, i.e. $\mathbf{u}_{nm} = 0$. This allows for more in-depth insight into the mechanical characteristics of potential tails to be made. As such, $\mathbf{u}_p = \mathbf{u}_{ank}$ in this work with values of $\kappa_p = 494$ Nm $\cdot$ rad^{-1} and $\kappa_d = 30$ Nm $\cdot$ s $\cdot$ rad^{-1} in line with [23].

2.4 Dynamic Manipulability . An assessment methodology is required to compare differing kinematic supernumerary tails. Equation (3) indicates that the generalised inertia matrix $\mathbf{M}_q$ is paramount in shaping the response of a system and how control inputs are mapped. Dynamic manipulability measures have been proposed to indicate the feasible operational space accelerations that generalised actuator forces create in joint space. Azad et al. [28] proposed the bounded-torque weighting matrix to assess the role of actuators in the manipulability of a particular point of a robot. This is applicable to SRTs whereby the CoM of the global system (human and tail) is the point of interest.

The kinematic mapping of the twist $\mathbf{t}$ of a point (i.e. the spatial velocity) in terms of the rates of the generalised co-ordinates $\dot{\mathbf{q}}$ is given via the Jacobian relationship, i.e.

$$\mathbf{t} = \mathbf{J}\dot{\mathbf{q}} \tag{7}$$

Substituting Eq. (7) into Eq. (3), the dynamical equation can be written in operational space as

$$\dot{\mathbf{t}} = -\mathbf{J}\mathbf{M}_q^{-1}\left(\mathbf{C}_q + \mathbf{G}_q\right) + \mathbf{J}\mathbf{M}_q^{-1}\mathbf{u} = \dot{\mathbf{t}}_{cg} + \mathbf{J}_t\mathbf{u} \tag{8}$$

where $\dot{\mathbf{t}}_{cg}$ is the operational acceleration due to gravitational and centripetal/Coriolis effects and $\mathbf{J}_t = \mathbf{J}\mathbf{M}_q^{-1}$.

Using Eq. (8), a manipulability ellipsoid can be defined with manipulability matrix [28]

$$\mathbf{\Lambda} = \mathbf{J}_t\mathbf{W}^{-1}\mathbf{J}_t^T \tag{9}$$

where $\mathbf{W}$ is a $k \times k$ weight matrix that applies a unit weighted norm on the actuators of the system. The axes of this ellipsoid are the eigenvalues λ of $\mathbf{\Lambda}$. From definition of $\mathbf{J}_t$, it is evident that λ are dependent on the kinematic and inertial properties of the system and thus will provide meaningful insight into the mechanical characteristics of potential SRTs to augment human balance.

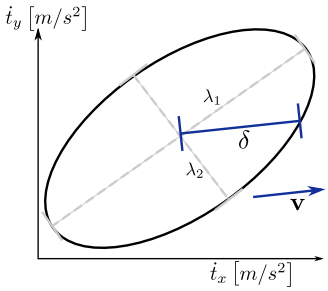

Fig. 2 The manipulability ellipsoid associated with a weight matrix W that has bounds on maximum torques of the actuators. The ability of the actuators to accelerate the system in the direction v is shown as the distance δ while the major and minor axes of the ellipsoid associated with eigenvalues λ of $\mathbf{\Lambda}$ are [28]

Nevertheless, the manipulability ellipsoid is also dependent on the selection of the weighting matrix $\mathbf{W}$ [28]

$$\mathbf{W} = \frac{1}{k}\mathtt{diag}\left(\left[\frac{1}{u_{1max}^2} \cdots \frac{1}{u_{kmax}^2}\right]\right) \tag{10}$$

which represents a bound on the maximum available torque for each of the k actuators. This selection models that each actuator has it's own characteristics, i.e. the ankle has a maximum torque it is capable of producing due to physiology whilst the actuators of a SRT are chosen based on a specification.

Typically, it is desired to accelerate a robot between two points in a particular direction $\mathbf{v}$. This can be ascertained from the manipulability ellipsoid, i.e. the distance from the centre of the ellipsoid to the intersection point on its surface in the desired direction as illustrated in Fig. 2. The following distance metric can be derived [28],

$$\delta = \frac{\|\mathbf{v}\|}{\sqrt{\mathbf{v}^T\mathbf{\Lambda}^{-1}\mathbf{v}}} \tag{11}$$

which is the maximum acceleration in the desired direction physically achievable with the actuator combination. Along with the eigenvalues λ of $\mathbf{\Lambda}$, δ will allow for a quantitative comparison to be made between SRTs .

3 One-dof Tails

Three potential one-dof SRTs are proposed; a linear counter mass (LCM), reaction wheel (RW) and swinging arc (Arc) tails as illustrated in Fig. 3 with the RW taking inspiration from [13,14] and Arc from [16]. In particular, interest lays in the method upon which the three proposed kinematic structures of the tails augment human balance and if an optimal structure exists. The three concepts all entail a fixed length posterior mounting. The LCM tail consists of a rail mounted perpendicular to the human's trunk. A mass slides along the rail to create the counter-balance torque. The RW concept is similar to the LCM; however, at the distal end a reaction wheel is attached that uses the principle of precession to create the counter-acting torque. The Arc concept attaches to the trunk via a revolute joint to create a swinging arc to counteract the instability induced by gravity.

3.1 Parameter and Frame Assignment . The parameters of the three one-dof robotic tails are illustrated in Fig. 3. For the linear counter mass and reaction wheel tails, the fixed rail is considered to be kinematically part of the same rigid body as the human. The rail is of length l_t, mounted at a height h_t and of mass m_t. For the LCM, a moving frame $\mathcal{F}_2$ is attached to the counter mass which is modelled as a point mass m_c, i.e. $I_c = 0$, and has a stroke of

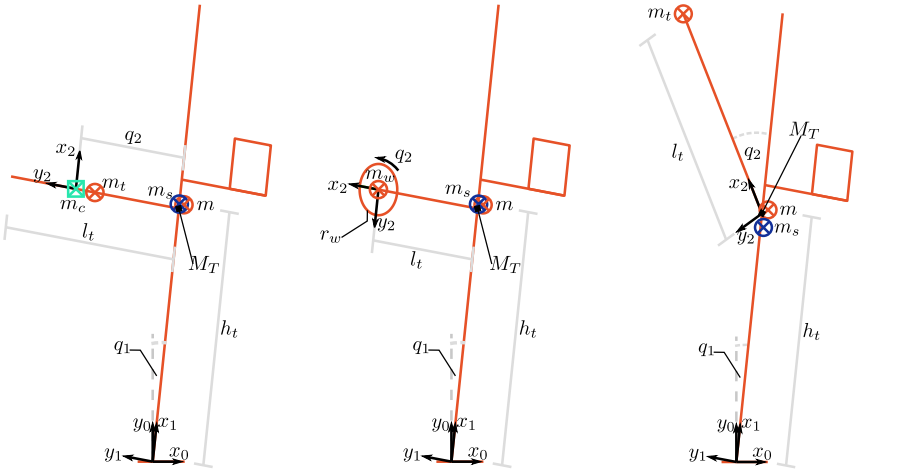

(*a*) Linear Counter Mass (LCM) SRT: linear motion of a sliding counter mass m_c counters the unstable gravitational torque

(*b*) Reaction Wheel (RW) SRT: the principle of precession spins a wheel of mass m_w to counter the gravitational torque

(*c*) Arc SRT: rotational motion of a swinging limb of mass m_t counters the unstable gravitational torque

Fig. 3 The three one-dof supernumerary robotic tails (SRTs) with their associated kinematic parameters, where q_1 and represents the ankle angle and q_2 the controlled variable of the tail. Centre of Mass (CoM) of the individual segments and overall system are indicated as orange and blue ⊗ respectively.

length d_c. The RW tail has moving frame assigned at the origin of the wheel of fixed radius r_w and mass m_w. The arc tail is mounted on the human at height h_t, with length l_t and mass m_t with the moving frame $\mathcal{F}_2$ assigned at the mounting point. The transformation ${}^1\mathbf{T}_2$ and values associated with the mass, inertia and fixed length parameters used in simulation for the three one-dof tails are tabulated in Table 2. The matrices associated with Eq. (3), i.e. $\mathbf{M}_q$, $\mathbf{C}_q$ and $\mathbf{G}_q$, along with the kinematic model given by the Jacobian relationship of Eq. (7) are provided in [Supplemental Material pdf].

Table 2 The geometric and mass parameters for the three one-dof SRTs with respect to Fig. 3. Distances have units of metres and mass in kilograms; $c_i = \cos q_i$,$s_i = \sin q_i$

Tail	Geometric	Mass	${}^1\mathbf{T}_2$
LCM	$h_t = 0.997$ $l_t = 0.9$	$m_t = 1$ $m_c = 4$ $I_t = \frac{m_t {l_t}^2}{12}$	$\begin{bmatrix} 1 & 0 & h_t \\ 0 & 1 & d_c \\ 0 & 0 & 1 \end{bmatrix}$
RW	$h_t = 0.997$ $r_w = 0.1$	$m_t = 1$ $m_w = 4$ $I_w = \frac{m_w {r_w}^2}{2}$	$\begin{bmatrix} -s_2 & -c_2 & h_t \\ c_2 & -s_2 & l_t \\ 0 & 0 & 1 \end{bmatrix}$
Arc	$h_t = 0.997$ $l_t = 0.9$	$m_t = 5$ $I_t = \frac{m_t {l_t}^2}{3}$	$\begin{bmatrix} c_2 & -s_2 & h_t \\ s_2 & c_2 & 0 \\ 0 & 0 & 1 \end{bmatrix}$

3.2 Stationary Point . The linearisation of the dynamics of the human-tail systems requires an appropriate stationary point to be defined. With respect to the SIP model of human stance and Fig. 1, upright posture correlates to an ankle angle $\bar{q}_1 = 0$. Enforcing static balance of gravitational torques about the ankle; the stationary point for the linear counter mass, reaction wheel and arc tails respectively are

$$m_c \bar{q}_2 = m_a l_a + m_l l_l - \frac{1}{2} m_t l_t \tag{12a}$$

$$\left(m_w + \frac{1}{2} m_t\right) l_t = m_a l_a + m_l l_l \tag{12b}$$

$$m_t l_t \sin \bar{q}_2 = m_a l_a + m_l l_l \tag{12c}$$

It is clear that for the LCM and Arc, the stationary value $\bar{q}_2$ is explicitly evident in Eqs. (12*a*) and (12*c*), and a unique solution in terms of the geometric and mass parameters can be determined which is not the case for the RW, i.e. Eq. (12*b*). This is due to the kinematic nature of the tail, a spinning wheel at a fixed point, and hence the associated stationary point $\bar{q}_2$ is 0. However, a design constraint on the mass of the wheel and the length of the tail is enforced, i.e. not both can be explicitly defined. Hence, the mass m_w is selected and l_t abides Eq. (12*b*). This does not mean a different length of RW tail is not possible; it theoretically implies that if a value of l_t that does not satisfy Eq. (12*b*) is chosen, the wheel will need to be spinning, i.e. $\dot{\bar{q}}_2 \neq 0$. Further, from Eq. (12*c*) a design constraint is imposed on the mass of the arc tail i.e. $m_t l_t \geq m_a l_a + m_l l_l$. Hence, it is clear that in the design of a one-dof SRT, the parameters must obey design constraints which are dependent on the mass of the load being held and its distance from the torso. Further, from a quiet standing perspective there is a unique pose of the human-tail system to maintain static balance.

3.3 Simulation and Assessment . A simulation was conducted to assess the performance of the three one-dof robotic tails to balance a human. The parameters of the human and tail utilised are as tabulated in Tables 1-2. Research has shown that 10 kg or greater mounted at the pelvis can be detrimental to the motion of a human [29]; hence, the total mass of the augmenting tails was set at 5 kg with fixed length of 0.9 m. Full state feedback controllers were developed to regulate the system to the stationary point. The specification of the closed loop behaviour was set to be the same for the three tails for comparison reasons. Specifically, a dominant pair of poles with settling time of 4 s and damping ratio 0.8,

with the non-dominant poles being placed 10 times away from the dominant pair.

The systems were simulated such that the CoM of the human was about to exceed the base of support. This correlated to an ankle angle $q_1 = 8°$ and the tails were held in the configuration that corresponds to their stationary point. Hence, $\mathbf{x}_0 = [8, 0, 0, 0]^T$. The time domain profile of the ankle for the three SRTs is shown in Fig. 4. It is evident that the linear counter mass and arc tails result in relatively smooth transition in ankle angle back to upright stance. However, for the reaction wheel tail, there is a large negative displacement of the ankle before the system settles back at the stationary point.The global system CoM, illustrated in Fig. 4, takes longer to settle for the Arc tail which is due to the rotational nature changing the y-coordinate of the tail's CoM. The motion of the human-tail systems can be viewed in [Supplemental Video]. The first two columns of Fig. 5 further reinforce these differences whereby the first column illustrates the displacement phase of the global CoM (i.e. total displacement the CoM undergoes from start to finish and associated velocity) and the second column the associated sagittal plane trajectory. As can be ascertained from these plots, the maximal linear velocity of the global CoM of the LCM and arc SRTs (0.6-0.75 ms^{-1}) and the displacement phase portraits are similar. However, the reaction wheel has a completely different phase portrait highlighting a significant lean of the global CoM backwards before heading towards the stationary point. Further, the system velocity is much larger than the other two tails for the same closed loop system specification, i.e. around -2.75 ms^{-1}.

The displacement phase results can be verified by the trajectory of the global CoM in the sagittal plane, shown in the second column of Fig. 5. From this, it can be seen that the RW system travels along the same path that created the lean before it settles at the stationary point whereas the LCM and Arc are more direct, i.e. they travel to the stationary point in a more efficient manner. The difference between the trajectories of the three tails to the stationary point is significant in terms of human balance. While the arc and linear counter mass systems undergo around 0.15 m CoM displacement from start to finish, the reaction wheel has a maximal displacement of 0.3 m from the rest point, and traverses back and forth. This instigates a backward lean which would physically lead to a human falling, i.e. the path is extremely undesirable and unsafe.

The previous analysis did not assess the motion of the three one-dof SRTs. Due to the kinematic dissimilarity of the tails a unified approach for comparison is required. The third and fourth columns of Fig. 5 illustrate the motion that the CoM of the three tails undertake, i.e. the displacement phase orbit of the CoM and the trajectory in the sagittal plane respectively. Considering the phase orbit plots, the displacement from the initial configuration is lowest for the reaction wheel, then the arc and linear counter mass. This is to be expected as the CoM of the RW does not change location with respect to the human body. Contrary to the global CoM, the velocity of the tails was higher for the LCM and Arc while the reaction wheel CoM had the same magnitude angular velocity as its CoM which is kinematically expected. Further, the displacement orbit of the RW is essentially identical to the global CoM. For the LCM and Arc, the counter mass travels further from the rest point than the arc (1.6 against 1.4 m) and both follow essentially a clockwise periodic transition from start to finish.

The sagittal plane trajectory of the tails undergo greatly different paths as can be seen in column 4 of Fig. 5. In this figure, the trajectory of two key points are also shown, correlating to key physical landmarks that the CoM of the tail cannot cross. For the reaction wheel and arc tail, these two points are the CoM of the human and the head; whilst for the LCM, they are the CoM of the human and the distal end of the rail. What can be ascertained from the trajectory plot of the tail CoMs is that the RW and Arc do not collide with the body to balance the system. However, the counter mass slides off the end of the rail, requiring large displacement to balance the system. Hence, whilst the linear counter mass option provides an efficient path of the global CoM to the stationary

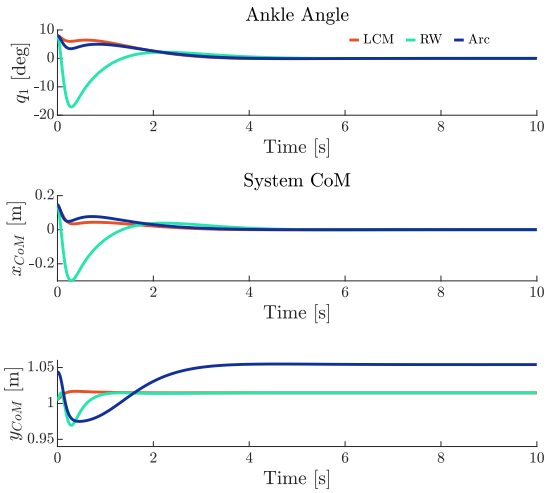

Fig. 4 Ankle (top) and global cartesian system CoM (middle-bottom) profiles stabilised with the Linear Counter Mass (LCM), Reaction Wheel (RW) and Arc SRTs

point, it does so by violating physical constraints. This observation coupled with the reaction wheel inducing a significant tilt back to provide balance, means the Arc SRT is the optimal one-dof robotic tail to augment human balance.

The prior discussion focussed on the kinematic aspects of the tails. To properly understand those results and the underlying ability to augment human balance with an active tail, it is imperative to investigate the dynamics of the systems utilising manipulability analysis. As the ankle is greater at producing plantar-flexion moments (average of around 100 Nm for an adult), the average dorsi-flexion value of 30 Nm [30] was selected to represent the passive capabilities of the ankle in the manipulability assessment. Assuming an appropriate transmission can be designed, the actuators of the tail were assumed to have maximums correlating to this, i.e. for the RW and arc 30 Nm and 30 N for the LCM.

Manipulability ellipses were assessed according to the initial condition and pose of the previous simulations. Figure 6 illustrates the configuration of the three human-tail systems and the associated manipulability ellipses, with Table 3 reporting the eigenvalues of the manipulability matrix $\mathbf{\Lambda}$, the distance δ and associated dynamic and Jacobian matrices. For this analysis, δ was in the direction that originated in the pose that was about to exceed the BoS towards the desired pose of upright stance, i.e. ability to accelerate in a straight line. It is evident that the potential for the LCM and RW tails to accelerate the CoM in multiple directions is diminished as the ellipses are straight lines. Further, as their $\delta = 0$, it is not possible to directly accelerate towards upright stance, irrespective of control law. However, the arc SRT has two non-zero eigenvalues, defined manipulability ellipse and is capable to accelerate to upright stance.

Clearly the reason for the difference in the trajectory response and manipulability is due to the kinematic structure $\mathbf{J}$ and the dynamics via the generalised inertia $\mathbf{M}_q$. From investigation of Jacobian matrices in Table 3, it can be seen that the second column of $\mathbf{J}$ for the reaction wheel is $\mathbf{0}$, i.e. the Jacobian is singular for all configurations and the twist of the CoM is independent of the angular velocity of the reaction wheel. This is not the case for the LCM and arc. Investigating $\mathbf{M}_q$, the coupling inertia term (off-diagonal) is of particular interest as it links the motion between the rigid bodies. For the LCM and RW, these terms are constant i.e. they are dependent on the design parameters and independent of configuration. For the LCM, this depends on the counter-mass or the height of the mounting point while for the RW it is dependent on the inertia of the wheel, i.e. its radius and mass [Supplemental Material pdf]. For the arc SRT, the coupling inertia term varies with the configuration of the tail. Therefore, it can be deduced that

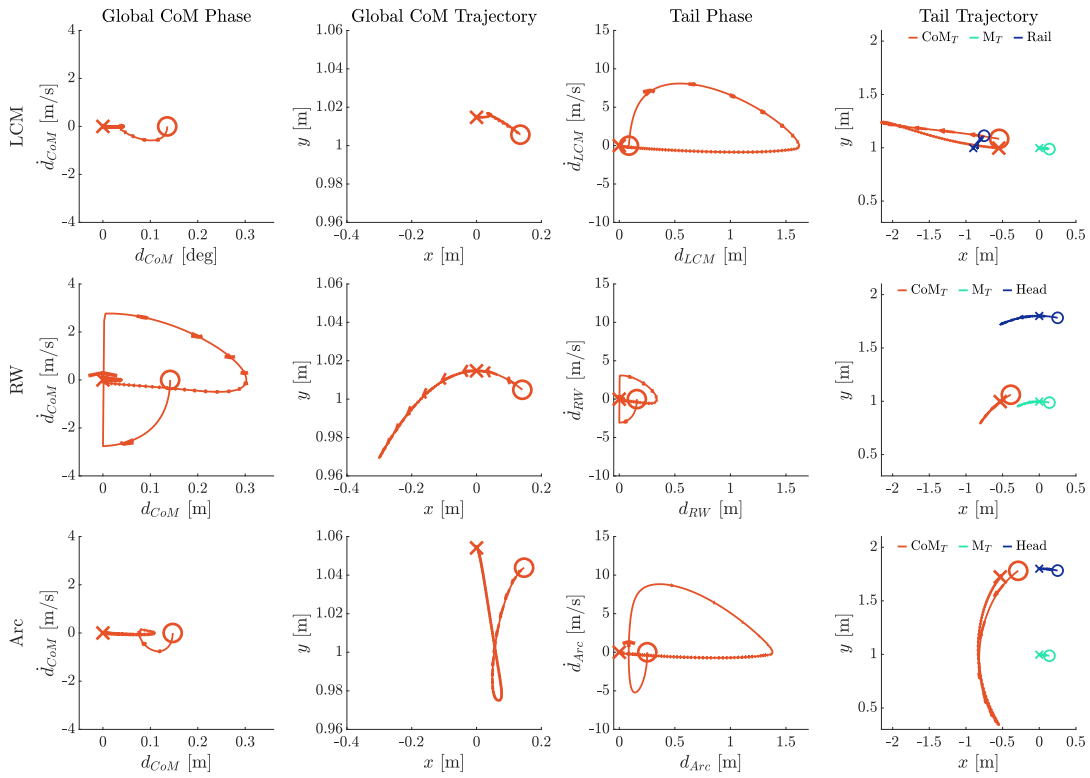

Fig. 5 Comparison of the displacement and trajectory orbits of the three one-dof SRT systems. Top-bottom: Linear Counter Mass (LCM); Reaction Wheel (RW); Arc. From (l-r): displacement orbit of the global CoM; sagittal plane trajectory of global CoM; displacement orbit of the tail CoM; sagittal plane trajectory of tail CoM and key physical landmarks (M_T are marked in Fig. 3). The ∘ and × indicate the start and finish points, respectively.

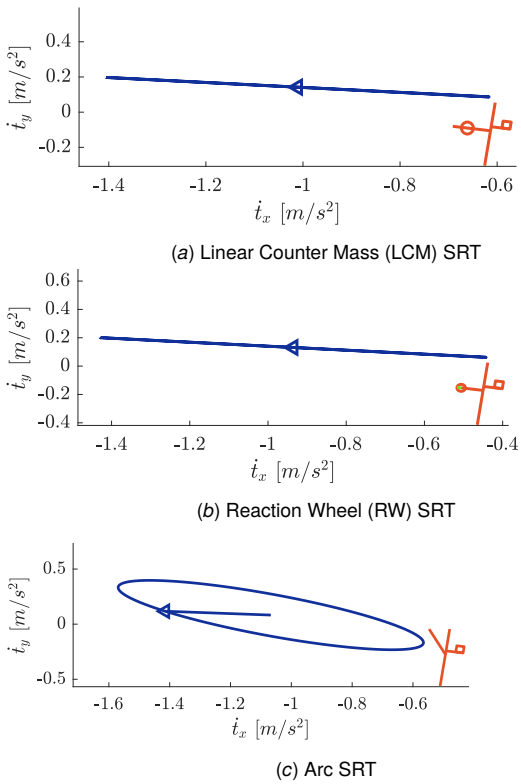

(*a*) Linear Counter Mass (LCM) SRT

(*b*) Reaction Wheel (RW) SRT

(*c*) Arc SRT

Fig. 6 Manipulability ellipses of the one-dof SRTs when at an ankle angle $q_1 = 8°$ (inset shows configuration).

variable coupling inertia is critical for a supernumerary robotic tail as it creates an efficient reaction force between the tail and human body. However, maximising this reaction force could have consequences on the human body. Overall, the manipulability analysis has provided theoretical reasoning to why the arc tail is the optimal one-dof SRT for augmenting human balance.

4 Two-dof Tails

Based on the analysisin the previous section, the two-dof supernumerary tails investigated in this section are limited to planar SRTs with revolute joints. These are a planar two-dof serial linkage (PS2), and the closed loop five bar linkage (FB). Rotational motion is used to counteract gravity effects; however, the serial versus closed-loop structure of the two tails mean differing workspace and force capabilities which could alter the ability to augment balance.

4.1 Parameter and Frame Assignment . The kinematic structure and parameters of the two-dof tails are illustrated in Fig. 7. The PS2 tail is an extension of the arc tail with an extra link attached by an actuated revolute joint to the distal end of the first. The tail is mounted on the human at height h_t, with lengths l_{ti} and mass m_{ti}, $i = 1, 2$. Frame $\mathcal{F}_2$ is assigned at the mounting point to the human and $\mathcal{F}_3$ at the revolute joint connecting the two tail segments. The five-bar SRT consists of two PS2 limbs which are connected via a revolute joint at the free ends; forming a closed loop. As the five-bar linkage has two-dof, only two of the joints are actuated with the others passive. With respect to Fig. 7(*b*), joints corresponding to angles q_{ia} are actuated and q_{ib} passive ($i = 2, 3$). The first limb of the five-bar tail is mounted at a height h_t and the second a further distance d_3 away. For both two-dof tails, the links' mass is distributed at their respective midpoints ,

Table 3 Dynamic manipulability assessment of the three one-dof SRTs

Tail	$\delta\,[ms^{-2}]$	$\lambda\,[ms^{-2}]$	$\mathbf{M}_q$	$\mathbf{G}_q$	$\mathbf{J}$
LCM	0	$\lambda_1 = 0.398$ $\lambda_2 = 0$	$\begin{bmatrix} 109.1 & 3.988 \\ 3.988 & 4 \end{bmatrix}$	$\begin{bmatrix} -111.5 \\ 5.461 \end{bmatrix}$	$\begin{bmatrix} -1.005 & -0.043 \\ 0.141 & 0.006 \end{bmatrix}$
RW	0	$\lambda_1 = 0.498$ $\lambda_2 = 0$	$\begin{bmatrix} 109.1 & 0.02 \\ 0.02 & 0.02 \end{bmatrix}$	$\begin{bmatrix} -113.9 \\ 0 \end{bmatrix}$	$\begin{bmatrix} -0.8962 & 0 \\ 0.1259 & 0 \end{bmatrix}$
Arc	0.3491	$\lambda_1 = 0.568$ $\lambda_2 = 0.169$	$\begin{bmatrix} 120.6 & 9.020 \\ 9.020 & 5.4 \end{bmatrix}$	$\begin{bmatrix} -132.7 \\ -20.87 \end{bmatrix}$	$\begin{bmatrix} -1.044 & -0.043 \\ 0.147 & -0.0231 \end{bmatrix}$

i.e. $I_i = \frac{1}{12} m_i {l_i}^2$, with mass of a two-dof PS2 limb obeying

$$m_i = \frac{l_j m_t}{l_i + l_j} \qquad m_j = \frac{l_i m_t}{l_i + l_j} \tag{13}$$

for $(i, j) = (t1, t2), (2a, 2b), (3a, 3b)$. The frame transforms and values of the physical parameters are tabulated in Table 4.

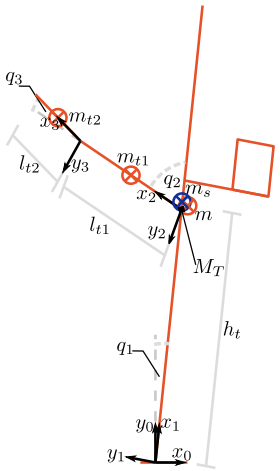

(*a*) Planar Serial Two-dof (PS2) SRT: rotational motion of a two-dof planar linkage with controlled angles q_2 and q_3 alter the CoM of the tail to counter the unstable gravitational torque

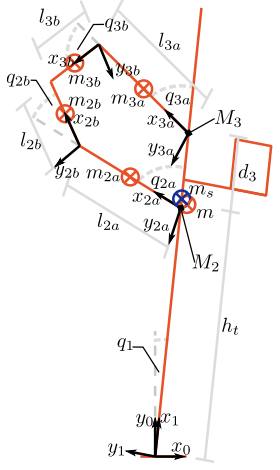

(*b*) Five Bar (FB) SRT: a closed loop linkage consisting of four segments with controlled angles q_{2a} and q_{3a} (q_{2b}, q_{3b} are passive). The combined CoM of the tail segments are used to counter the unstable gravitational torque.

Fig. 7 The kinematic parameters of the two-dof SRTs where the CoM of the individual segments and overall system are indicated as orange and blue ⊗ respectively.

The open loop kinematic structure of the PS2 tail means that the CoM Jacobian and inverse dynamic model are readily derived using elementary techniques. For the five-bar tail, the closed loop imposes kinematic constraints. Whilst the CoM Jacobian can be readily derived in terms of all the joint rates of the system, the passive joint rates should be determined in terms of the active rates. As such, the dynamics of the five-bar SRT should be derived solely in terms of the active joint rates. The dynamic matrices related to Eq. (3) for the two-dof SRTs and algorithm to obtain the dynamics of the five-bar SRT are provided in [Supplemental Material pdf].

4.2 Stationary Point . For the one-dof robotic tails, a unique stationary point is achieved given prescribed values for tail lengths and mass. With two-dof SRTs, the CoM of the tails are

$${}^0\mathbf{s}_{PS2} = \frac{m_{t1}\,{}^0\mathbf{s}_{t1} + m_{t2}\,{}^0\mathbf{s}_{t2}}{m_{t1} + m_{t2}} \tag{14a}$$

$${}^0\mathbf{s}_{FB} = \frac{m_{2a}\,{}^0\mathbf{s}_{2a} + m_{2b}\,{}^0\mathbf{s}_{2b} + m_{3a}\,{}^0\mathbf{s}_{3a} + m_{3b}\,{}^0\mathbf{s}_{3b}}{m_{2a} + m_{2b} + m_{3a} + m_{3b}} \tag{14b}$$

where ${}^0\mathbf{s}_i$ are the position co-ordinates of the CoM of body i. Generalising the x and y co-ordinates of Eq. (14) as s_x and s_y respectively, the static balance equation is

$$s_x = -\frac{m_a l_a + m_l l_l}{m_t} \tag{15}$$

i.e. the x-coordinate of the tail's CoM is defined.

Despite s_x being completely defined by Eq. (15); from Eq (14) it is clear the transformation to joint space is not unique, i.e. there are multiple stationary points due to the kinematic redundancy of the extra-dof. Hence, the y-coordinate of the tail CoM is free to be positioned as a result. This is a significant advantage over the one-dof tails, as it allows for adaptation of an SRT to different environments and flexibility in the selection of the length and mass of the tail segments. A selection criteria is required to select stationary points which can be based on workspace environment , dynamic manipulability in a neutral position or the configuration that has maximal acceleration in a particular direction δ given by Eq. (11). However, solving for suitable stationary points of the two proposed two-dof SRTs is not a trivial exercise with the algorithms used provided in [Supplemental Material pdf].

4.3 Simulation and Assessment. Simulation of the two-dof supernumerary tails was conducted using the parameters in Tables 1 and 4. The length of the PS2 limbs was chosen to sum to 0.9 m, consistent with the length of the one-dof arc and LCM tails. The segments closest to the human body were set to be twice the length of the distal tail segments. Similarly, the total mass of the segments of the two-dof SRTs was chosen to be 5 kg as with the one-dof cases. The mass distribution between tail segments was chosen to bias the tail CoM towards the distal end, i.e. the distal segments of tails were heavier, obeying Eq. (13).

Table 4 The geometric and mass parameters for the two-dof SRTs with respect to Fig. 7. Distances have units of metres and mass in kilograms

Tail	Geometric	Mass	${}^{i}\mathbf{T}_{j}$
PS2	$h_t = 0.997$ $l_{t1} = 0.6$ $l_{t2} = 0.3$	$m_{t1} = 1.667$ $m_{t2} = 3.333$	${}^{1}\mathbf{T}_{2} = \begin{bmatrix} c_2 & -s_2 & h_t \\ s_2 & c_2 & 0 \\ 0 & 0 & 1 \end{bmatrix}$ ${}^{2}\mathbf{T}_{3} = \begin{bmatrix} c_3 & -s_3 & l_{t1} \\ s_3 & c_3 & 0 \\ 0 & 0 & 1 \end{bmatrix}$
FB	$h_t = 0.997$ $d_3 = 0.3$ $h_2 = h_t$ $h_3 = h_t + d_3$ $l_{ia} = 0.6$ $l_{ib} = 0.3$	$m_{ia} = 0.8333$ $m_{ib} = 1.667$	${}^{1}\mathbf{T}_{ia} = \begin{bmatrix} c_{ia} & -s_{ia} & h_i \\ s_{ia} & c_{ia} & 0 \\ 0 & 0 & 1 \end{bmatrix}$ ${}^{ia}\mathbf{T}_{ib} = \begin{bmatrix} c_{ib} & -s_{ib} & l_{ia} \\ s_{ib} & c_{ib} & 0 \\ 0 & 0 & 1 \end{bmatrix}$

To allow for comparison with the one-dof cases, the same initial condition scenario was utilised, i.e. an ankle angle $q_1 = 8°$ and the tails held in the configuration of the stationary point. The dynamic manipulability metric δ given by Eq. (11) was used to select the staionary point, i.e. configuration with the greatest ability to accelerate the global CoM from the initial condition of $q_1 = 8°$ to $q_1 = 0°$. With the addition of a dof, the two-dof SRT system equations have 6 states opposed to 4 of the one-dof tails. For comparison with the one-dof cases, the dominant pair of poles was chosen the same, i.e. settling time of 4 s and damping ratio 0.8. Two pairs of non-dominant poles were specified at being 5 and 10 times away from the dominant pair. Full state feedback controllers were developed according to the theory in [31]. Bounds were applied on the states related to the actuators of the tails to ensure that the tails did not interfere with the human body, and limitations associated with local linearisation of highly non-linear dynamical systems. The PS2 limits were set at $q_{(2,3)lim} = [-80°, 80°]$ and the FB at $q_{2a,lim} = [-12.5°, 25°]$, $q_{3a,lim} = [-25°, 12.5°]$.

The time domain profile the ankle undergoes with the two-dof SRTs is shown in Fig. 8. Both tails engage in a smooth transition of the ankle from the initial condition back to upright stance. Compared to the one-dof tails, the profile is more ideal as there are no lean forwards/backwards or deviations that are evident with the one-dof SRTs. Further, both two-dof SRTs allow for the ankle angle to settle quicker than the one-dof tails, i.e. the primary objective of upright stance is achieved more efficiently with the two-dof SRTs. This is also the case for the x-coordinate of the global CoM. Within the two-dof SRTs, it can be ascertained from Fig. 8 that the five-bar tail allows for the ankle angle to return to its stationary point in shorter duration than the PS2 tail. The motion of the two-dof systems can be viewed in [Supplemental Video].

Investigating the first two columns of Fig. 9 allows for insight into the trajectory undertaken by the global CoM. With respect to the displacement phase plot in the first column, it can be asserted that both tails undergo essentially the same overall displacement of the global CoM, around 0.15 m. This is consistent with the one-dof SRTs and is to be expected as the systems all start and finish in the same configuration with respect to the dominant body, the human. Whilst the one-dof SRTs undergo a continuous trajectory from start to finish, the two-dof tails do not, as can be seen in the second column of Fig. 9. For both tails, there is an initial acceleration of the CoM before a sudden stop and change in direction. Intuitively, these sudden stops coincide with reaching the limits on the range of motion of the joint(s) of the tail. Further, these

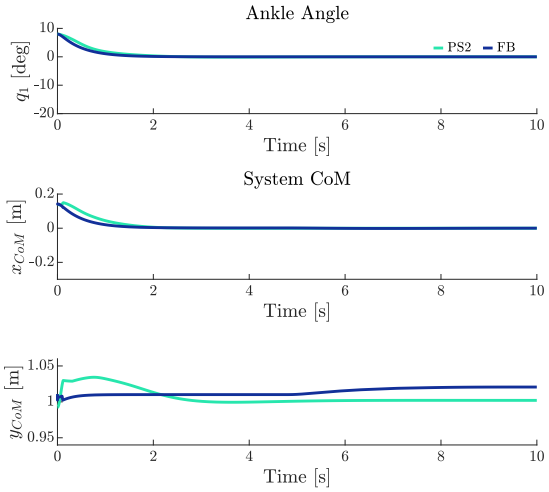

Fig. 8 Ankle (top) and global cartesian system CoM (middle-bottom) profiles stabilised with the Planar Serial Two-dof (PS2) and Five-Bar (FB) SRTs

changes in directions of the global CoM are reflected as spikes in the displacement phase plots in column one which are not apparent for the one-dof SRTs.

Nevertheless, whilst the one-dof tails incorporate a lean or tilt opposing the desired direction of global CoM motion (i.e. the loop in the trajectory plots of the LCM and arc SRTs), the two-dof Human-Tail systems go from start to finish in a relatively smooth manner, i.e. motion pointed from the start to finish point throughout. Further, it can be gathered from the global CoM trajectory that the five-bar SRT has essentially decoupled returning to the state of upright stance, and returning the tail to its stationary configuration. This is apparent as the global CoM reaches an x-displacement of 0 (i.e. upright stance) before the final resting point, with the trajectory traversing the y-axis in the final stages. This can be attributed to the limits enforced on the FB tail joints; essentially showing there is sufficient momentum and holding torque to achieve upright stance even if the tail is held stationary for a period. Contrarily, the PS2 tail has a more co-ordinated return to the stationary point. This can explain why the ankle angle settles quicker with the five-bar SRT than the PS2.

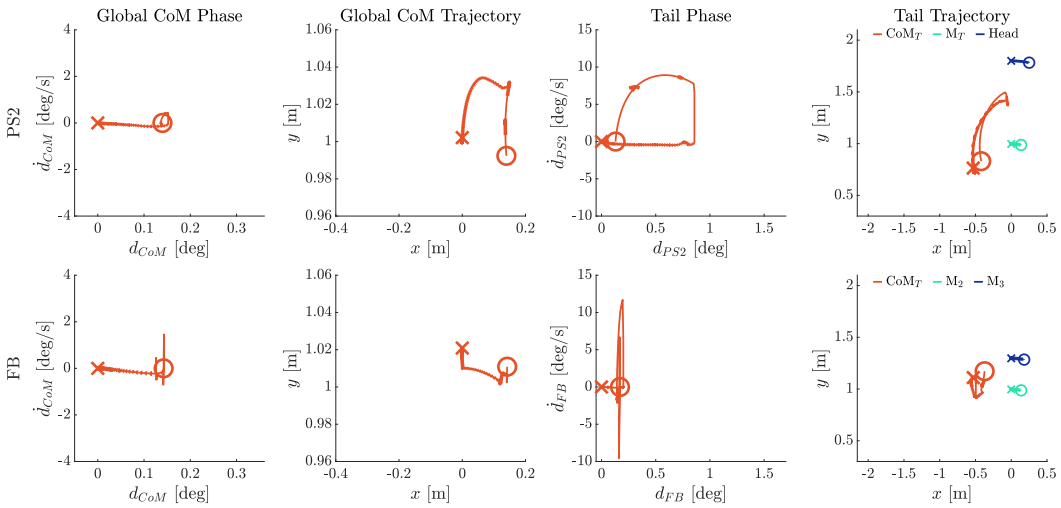

Fig. 9 Comparison of the phase and trajectory orbits of the two-dof SRT systems. Top-bottom: Planar Serial Two-dof (PS2); Five-Bar Linkage (FB). From (l-r): displacement orbit of the global CoM; sagittal plane trajectory of global CoM; displacement orbit of the tail CoM; sagittal plane trajectory of tail CoM and key physical landmarks (M_i are marked in Fig. 7). The ∘ and × indicate the start and finish points, respectively.

The respective motion of the two-dof robotic tails CoM to augment balance is illustrated by the displacement phase orbit and sagittal plane trajectory in the third and fourth columns of Fig. 9. From column three, the five-bar SRT almost immediately reaches two joint limits as indicated by the two spikes, i.e. the two independent limbs. The tail immediately reconfigures and provides a reactive moment to counter the gravitational torque. However, at around 0.2 m, another limit is reached and the tail is held in this pose as inferred from the velocity dropping to 0. The momentum in the system at this stage, however, is sufficient to account for the instability caused by gravity and motion continues towards upright stance. Comparatively, the PS2 tail changes its CoM in an initial arc like trajectory before reaching a joint limit as indicated by the velocity reaching 0. The braking of the PS2 tail does not cause the system to become unstable and upright stance is achieved. Further, the tails undergo similar levels of velocity; a maximum 8-10 ms^{-1}.

Scrutinising the overall displacement of the tail CoMs, there is a noticeable difference. The PS2 undergoes a maximum displacement from its final resting position at the stationary point of 0.86 m. The five-bar, however, has maximum tail CoM displacement of 0.2 m, i.e. it returns the system to the stationary point utilising 23% of the displacement of the PS2 tail. Investigating column four of Fig. 9 which shows the sagittal plane trajectory of the tail with key landmarks (Human CoM and Head for PS2; the tail mounting points for the FB), it can be seen that neither tails interfere with the body. Further, it can be seen that the five-bar SRT undergoes a smaller displacement; which is also valid when comparing to the one-dof cases. This phenomena of the two tails can be attributed to the properties of open versus closed loop mechanisms. Due to the kinematic structure, open-loop mechanisms naturally have a large workspace. However, the kinematic constraints imposed in a closed-loop linkage, makes the system more rigid. Thus, despite having a smaller working area, the added rigidity of a closed-loop linkage enhances its force generating capabilities. Hence, a reason why the FB tail requires a significantly smaller working area to augment balance compared to the PS2.

To gain further insight into the two-dof tails, dynamic manipulability was assessed according to the initial condition and pose of the previous simulations. The ankle torque was set at 30 Nm with the two actuators of the tail set at 15 Nm, i.e. the value used for the one-dof SRTs was distributed between the two actuators. The manipulability ellipses of the PS2 and five-bar SRTs are shown in Fig. 10 with the eigenvalues of the manipulability matrix $\mathbf{\Lambda}$, the acceleration metric δ (towards upright stance) and dynamic matrices tabulated in Table 5. Both tails have two non-zero eigenvalues associated with $\mathbf{\Lambda}$ and thus are able to directly accelerate towards the stationary point. The ability to do so is greater for the PS2 tail; 0.62 ms^{-2} opposed to 0.52 ms^{-2} for the FB tail; greater than the 0.349 ms^{-2} of the arc tail. Thus, the two-dof tails are more manipulable than the best one-dof option.

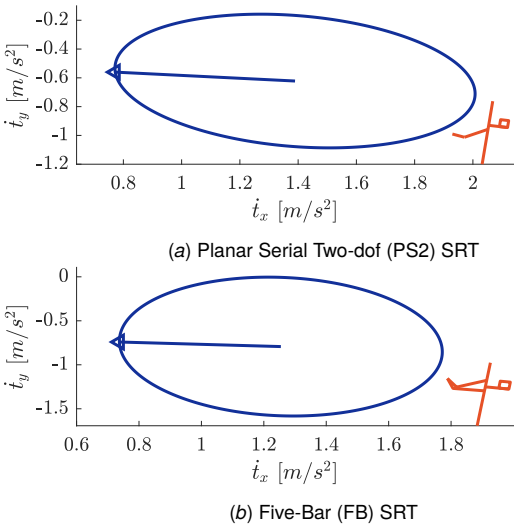

(*a*) Planar Serial Two-dof (PS2) SRT

(*b*) Five-Bar (FB) SRT

Fig. 10 Manipulability ellipses of the two-dof SRTs when at $q_1 = 8°$ (inset shows configuration).

It is not apparent from investigation of $\mathbf{M}_q$ and $\mathbf{J}$ that define $\mathbf{\Lambda}$ what causes the difference in available acceleration between tails. The pose of the tails were chosen to maximise acceleration of the global CoM towards the stationary point from the initial condition, i.e. the δ values reported are maximal for the specific configuration and direction. From Fig. 10, it can be seen that the acceleration in the desired directions are essentially along the major axes of the ellipses. This is verified from the eigenvalues λ of the two tails reported in Table 5. The major axis of the PS2 tail has length 0.631 ms^{-2}, i.e. the δ = 0.62 ms^{-2} is almost entirely along this axis. Comparatively, the major of the FB ellipse has length 0.791 ms^{-2} with the δ = 0.52 ms^{-2} slightly off this axis. For the minor of the two ellipses, the five-bar SRT is larger at 0.515 ms^{-2}

Table 5 Dynamic manipulability assessment of the two-dof SRTs

Tail	$\delta\,[ms^{-2}]$	$\lambda\,[ms^{-2}]$	$\mathbf{M}_q$	$\mathbf{G}_q$	$\mathbf{J}$
PS2	0.620	$\lambda_1 = 0.631$ $\lambda_2 = 0.446$	$\begin{bmatrix} 107.6 & -0.8 & -0.414 \\ -0.8 & 1.962 & 0.331 \\ -0.414 & 0.331 & 0.1 \end{bmatrix}$	$\begin{bmatrix} -126.1 \\ -27.4 \\ -4.675 \end{bmatrix}$	$\begin{bmatrix} -0.992 & 0.009 & -0.002 \\ -0.140 & -0.030 & -0.005 \end{bmatrix}$
FB	0.520	$\lambda_1 = 0.791$ $\lambda_2 = 0.515$	$\begin{bmatrix} 105.2 & -1.412 & 0.895 \\ -1.412 & 1.571 & -0.660 \\ 0.895 & -0.660 & 1.138 \end{bmatrix}$	$\begin{bmatrix} -135.6 \\ -17.64 \\ -6.334 \end{bmatrix}$	$\begin{bmatrix} 0.947 & -0.002 & -0.002 \\ -0.162 & -0.028 & -0.002 \end{bmatrix}$

against 0.446 ms^{-2} for the PS2. In general, manipulability of a configuration can be defined as the ratio of the eigenvalues, the closer to unity the more manipulable. Using this definition, the PS2 tail is superior to the five-bar tail, 1.415 to 1.536. However, the ratio does not take into account the acceleration magnitudes. In this respect, the five-bar has larger major and minor axes. Thus, with ankle angle of 8°, the PS2 tail has the greatest available acceleration to directly accelerate the global CoM to upright stance; however, the FB tail has greater manipulability to accelerate the global CoM in multiple directions due to its larger principal axes.

It was observed that the five-bar supernumerary tail achieves upright stance the quickest of the two-dof tails despite using 23% of the range of the PS2. From inspection of the gravity torque vector in Table 5, it also has larger gravity effects. However, it is the inertia matrix $\mathbf{M}_q$ that is critical, with the coupling inertia terms (i.e. off diagonals) close to 50% higher for the five-bar tail. This can be attributed to the kinematic structure, i.e. the closed loop of the five-bar increases the coupling inertia as the passive bodies are projected into the active space. A more rigid mechanism with greater force capabilities results, hence a reason why the FB tail achieves upright stance with a smaller motion than the PS2. Further, from Table 4, while the total mass of the two-dof tails are the same at 5 kg; the individual links of the FB tail are lighter than the PS2 counterparts. This implies that coupling inertia is not simply increased by utilising heavier links; it is heavily dependent on the kinematic mechanism.

The primary objective of this investigation was to gain insight into the mechanical characteristics of potential supernumerary robotic tails, not the most optimal way to automatically augment balance or actuator requirements. Hence, a simple LTI control allowed for useful comparison between designs. However, it is clear that from the results that a state regulator and pole placement specification is not the ideal controller for a robotic tail, particularly for the two-dof cases. To best use the redundant dof, a control law that makes use of the null-space of the system dynamics would be better which would allow for task-space trajectories between desired global CoM positions to be chosen. The redundancy can then be exploited to minimise the actuation requirements or a metric based on the kinematic or biomechanical state of the human.

A further issue with the state regulator concerns its suitability for the closed-loop five-bar SRT. The state regulator has no sense of the task-space configuration of the five bar mechanism, i.e. whether limb interference or a parallel singularity has occurred is not accounted for. As such, strict limits needed to be applied for the FB compared to the PS2; resulting in discontinuities in the trajectory. However, the results show that with more appropriate control, such discontinuities in the trajectory could easily be avoided.

4.4 Use Case Scenario. The open loop nature of the PS2 gives it an advantage in manufacture and control terms compared to the FB tail. As such, it is considered the most viable form of a potential supernumerary robotic tail for balance augmentation. The previous analysis was focussed on a large displacement of the ankle; however, the purpose of an SRT is to avoid such a position occurring. In all likelihood, such a displacement is caused via an external force disturbance. A potential scenario in which an SRT could be utilised is by industrial workers in a warehouse setting carrying loads. In the previous simulations, it was assumed that the wearer of the tail was holding a 5 kg load with the dynamics linearised about this point. As such, it can be assumed that this is considered 'comfortable' and the worker can maintain vertical posture. Consider the situation where extra load of mass m_+ is suddenly added to the existing load being held. This can be considered as an external disturbance located at the user's hand (i.e. a pure force) which can readily be transformed to an equivalent disturbance wrench $\mathbf{w}_d$ at the centre of mass of the system (i.e. the control point). Hence, the joint acceleration disturbance $\boldsymbol{\rho}$ is

$$\boldsymbol{\rho} = \mathbf{M}_q^{-1}\mathbf{J}^T\mathbf{w}_d \tag{16}$$

As such, the state space equation with disturbance is

$$\dot{\mathbf{x}} = \mathbf{A}\mathbf{x} + \mathbf{B}\mathbf{u} + \boldsymbol{\rho} \tag{17a}$$

$$\mathbf{y} = \mathbf{C}\mathbf{x} \tag{17b}$$

where $\mathbf{y}$ represents the output of the system.

A state feedback controller utilised in the previous formulation does not guarantee robustness against disturbances. Instead, consider augmenting the system with extra states $\mathbf{z}$ corresponding to the integral of the output equation, Eq. (17*b*), with respect to a desired reference trajectory $\mathbf{r}$, i.e.

$$\mathbf{z} = \int \mathbf{y} - \mathbf{r}dt = \int \mathbf{C}\mathbf{x} - \mathbf{r}dt \tag{18}$$

Considering the case of regulation ($\mathbf{r} = 0$), the augmented system can be expressed as

$$\begin{bmatrix} \dot{\mathbf{x}} \\ \dot{\mathbf{z}} \end{bmatrix} = \begin{bmatrix} \mathbf{A} & \mathbf{0} \\ \mathbf{C} & \mathbf{0} \end{bmatrix} \begin{bmatrix} \mathbf{x} \\ \mathbf{z} \end{bmatrix} + \begin{bmatrix} \mathbf{B} \\ \mathbf{0} \end{bmatrix} \mathbf{u} + \boldsymbol{\rho} \tag{19}$$

their are m inputs to the systems, at most m states can be accurately tracked. Hence, the dimension of the augmented state matrix in Eq. (19), is at most $n + m$. With respect to the SRT system and disturbance rejection, the variable to be regulated is the angle of the ankle with the tail joints required to reconfigure to new positions based on the added load m_+. As such, the output equation is chosen as $y = x_1$ and the dimension of the augmented system is 7, adding one integrator pole at the origin.

The results of load disturbance on the system are shown in Fig. 11 where the disturbance is considered to vary with time and position, i.e. it is not linearised. Two cases of added mass were simulated, $m_+ = 5$ (49.1 N) and 15 kg (147.2 N), with the heavier case correlating to a total of 20 kg being held by one human, i.e. the maximum occupationally recommended. As can be seen from Fig. 11(*a*), both scenarios result in large joint disturbance accelerations and the tail joints immediately react with corresponding velocity. This means that the limits of the tail are reached quickly, causing discontinuity in the trajectory. Further, it can be seen that once the impact of the disturbance settles, the first joint of the tail settles at a new position, the second tail joint is held at the limit,

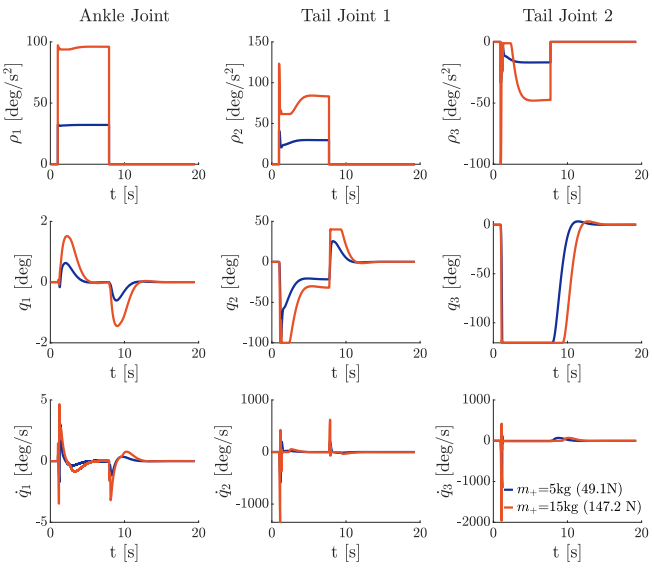

(*a*) Response of the system states when subjected to disturbance δ

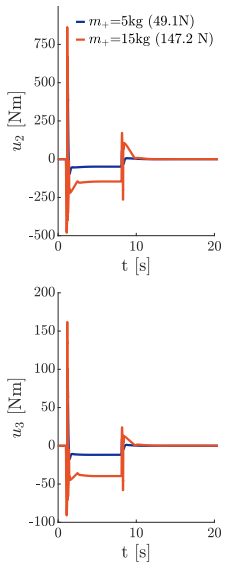

(*b*) Torque of the two tail actuators

Fig. 11 System response of the PS2 tail when an extra mass m_+ is held by the user

and the human is vertically upright. This new settled point is reflected by the system's global CoM changing when load is held, as illustrated in Fig. 12. Once the added mass is removed, the system settles back at the stationary point. These motions can be visualised in the [Supplemental Video].

The torque of the tail joints associated with the disturbance simulation is shown in Fig. 11(*b*). As can be seen, the torque profiles rapidly increase to large magnitude as a result of the large disturbances and consist of discontinuities due to the tail limits being encountered. Hence, unconventionally large power requirements are required utilising these simulations and control implementation as a design specification. Note, that in the SRT work of [16], a 200 W motor is used but torque requirements are not detailed. Further, series elastic actuators (SEAs) are commonly employed in the development of exoskeletons with Wang et al. [32] utilised SEAs capable of delivering 100 Nm of torque and 1 kW of power at each joint of an 8-dof exoskeleton. As such, the use of SEAs in the mechatronic design of an SRT is suggested. With respect to the simulations in Fig. 11(*b*), the large torque is two-fold. One reason is the actual formulation of the controller; actuation and control are intrinsically linked. State regulators do not allow for constraints on state variables and actuation limits to be directly embedded into the control problem; hence, hard limits are utilised which cause discontinuities that are amplified in control. An alternative to impose state constraints would be to utilise repulsive potential fields to prevent the tail reaching forbidden regions close to the human body. Further, model predictive control allows for limits in actuation to be built into the control problem which should be further explored for the control of an SRT.

It is to be noted that the human system modelled here is inherently unstable as only the mechanical stiffness of the ankle is considered. The velocity, gains and torque associated with the tail joints are thus larger than what would occur if infinite dimensional neural dynamics that stabilise upright human stance are included in control. Hence, these results show that consideration to such neural control capability is paramount to realise physically achievable design specification; particularly to align it with the 1 kW power of SEAs utilised by [32]. Given that humans are capable of naturally withstanding added loads and maintaining balance, the results show the remarkable power associated with the delayed neural controller. However, to account for this is not as simple as increasing proportional or derivative gains, as the delayed control implies that past history is utilised in a superposed way to create

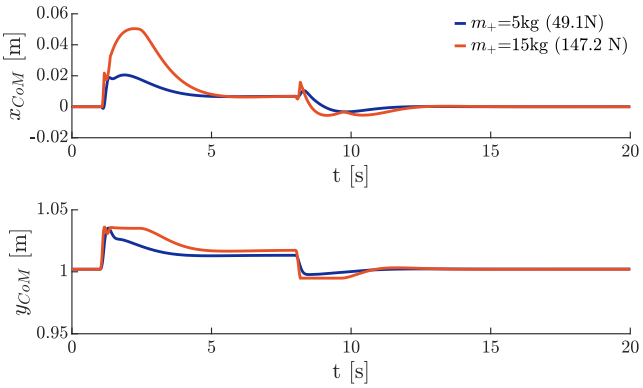

Fig. 12 Displacement of the global system centre of mass in a prototypical use case scenario of holding extra mass

added stabilisation torque [33]. As such, these simulations highlight and stress the need to correctly model human capabilities in the specification of wearable robotics as it can lead to reduced requirements. This is particularly important for control development and the correct specification of actuators, gearing transmissions, and the geometric-inertial parameters of the wearable system.

5 Conclusion

This investigation had a simple premise of determining the feasibility of a supernumerary robotic tail to augment human balance and its optimal kinematic structure. It is apparent that variable coupling inertia and rotational motion are imperative to counteract the gravitational torque; with two-dof SRTs being far superior than one-dof tails. However, the power requirements for an SRT are of concern, with consideration to the neural control that maintains human stability paramount to reduce overall design specification as well as the controller implemented.

It is imperative to minimise the overall mass and associated control units of the tail. Traditionally, moving inertia of robotic manipulators is minimised and base-mounted actuation is preferred. For a supernumerary tail, the human body acts as a floating base and moving inertia is critical to achieve balance. However, the aim of the design is to minimise the inertia applied to body. Hence, for

an SRT it would be ideal to incorporate the actuators and power supply (i.e. batteries) in the moving mass, requiring sophisticated thought in the mechatronic design phase.

This investigation utilised fundamental analysis techniques to determine the feasibility of augmenting human balance with a supernumerary robotic tail and the best mechanical form to do so. Through this, many key insights have been made which can be transferred to the design stage and future potential research avenues in the field of SRTs have been highlighted. This analysis is of particular importance for the design and development of physical human-robot interaction (pHRI) mechanisms, as it is imperative to minimise the impact such devices have on the human body. Hence, overall this work can lead to informed design of supernumerary robotic tails and be adopted in other avenues of mechanism development, particularly pHRI.

Acknowledgement

This work was supported by the UK Research and Innovation, Engineering and Physical Sciences Research Council under grant EP/T027746/1 'Automatic Posture and Balance Support for Supernumerary Robotic Limbs'. For the purpose of open access, the authors have applied a Creative Commons Attribution (CC BY) license to any Accepted Manuscript version arising. We sincerely thank Professor Etienne Burdet, Radhika Gudipati, Richard Walker and Zaheer Osman for valuable discussions on supernumerary robotic limbs and project support.

References

[1] World Health Organisation, 2021, "Step safely: strategies for preventing and managing falls across the life course," https://www.who.int/publications/i/item/978924002191-4.

[2] Park, J. H., Kim, S., Nussbaum, M. A., and Srinivasan, D., 2021, "Effects of two passive back-support exoskeletons on postural balance during quiet stance and functional limits of stability," Journal of Electromyography and Kinesiology, **57**, p. 102516.

[3] Maurice, P., Čamernik, J., Gorjan, D., Schirrmeister, B., Bornmann, J., Tagliapietra, L., Latella, C., Pucci, D., Fritzsche, L., Ivaldi, S., and Babič, J., 2020, "Objective and Subjective Effects of a Passive Exoskeleton on Overhead Work," IEEE Transactions on Neural Systems and Rehabilitation Engineering, **28**(1), pp. 152–164.

[4] Monaco, V., Tropea, P., Aprigliano, F., Martelli, D., Parri, A., Cortese, M., Molino-Lova, R., Vitiello, N., and Micera, S., 2017, "An ecologically-controlled exoskeleton can improve balance recovery after slippage," Scientific Reports, **7**, p. 46721.

[5] Zhang, T., Tran, M., and Huang, H., 2018, "Design and Experimental Verification of Hip Exoskeleton With Balance Capacities for Walking Assistance," IEEE/ASME Transactions on Mechatronics, **23**(1), pp. 274–285.

[6] Farkhatdinov, I., Ebert, J., van Oort, G., Vlutters, M., van Asseldonk, E., and Burdet, E., 2019, "Assisting Human Balance in Standing With a Robotic Exoskeleton," IEEE Robotics and Automation Letters, **4**(2), pp. 414–421.

[7] Hao, M., Zhang, J., Chen, K., Asada, H., and Fu, C., 2020, "Supernumerary Robotic Limbs to Assist Human Walking With Load Carriage," Journal of Mechanisms and Robotics, **12**(6), p. 061014.

[8] Khazoom, C., Caillouette, P., Girard, A., and Plante, J.-S., 2020, "A Supernumerary Robotic Leg Powered by Magnetorheological Actuators to Assist Human Locomotion," IEEE Robotics and Automation Letters, **5**(4), pp. 5143–5150.

[9] Gonzalez, D. J. and Asada, H. H., 2019, "Hybrid Open-Loop Closed-Loop Control of Coupled Human–Robot Balance During Assisted Stance Transition With Extra Robotic Legs," IEEE Robotics and Automation Letters, **4**(2), pp. 1676–1683.

[10] Kurek, D. A. and Asada, H. H., 2017, "The MantisBot: Design and impedance control of supernumerary robotic limbs for near-ground work," *2017 IEEE International Conference on Robotics and Automation (ICRA)*, pp. 5942–5947, doi: 10.1109/ICRA.2017.7989700.

[11] Parietti, F. and Asada, H., 2016, "Supernumerary Robotic Limbs for Human Body Support," IEEE Transactions on Robotics, **32**(2), pp. 301–311.

[12] Luo, J., Gong, Z., Su, Y., Ruan, L., Zhao, Y., Asada, H. H., and Fu, C., 2021, "Modeling and Balance Control of Supernumerary Robotic Limb for Overhead Tasks," IEEE Robotics and Automation Letters, **6**(2), pp. 4125–4132.

[13] Romtrairat, P., Virulsri, C., and Tangpornprasert, P., 2019, "An application of scissored-pair control moment gyroscopes in a design of wearable balance assistance device for the elderly," Journal of Biomechanics, **87**, pp. 183–188.

[14] Lemus, D., Berry, A., Jabeen, S., Jayaraman, C., Hohl, K., van der Helm, F. C. T., Jayaraman, A., and Vallery, H., 2020, "Controller synthesis and clinical exploration of wearable gyroscopic actuators to support human balance," Scientific Reports, **10**, p. 10412.

[15] Nabeshima, J., Saraiji, M. Y., and Minamizawa, K., 2019, "Arque: Artificial Biomimicry-Inspired Tail for Extending Innate Body Functions," ACM, pp. 1–2, doi: 10.1145/3306214.3338573.

[16] Maekawa, A., Kawamura, K., and Inami, M., 2020, "Dynamic Assistance for Human Balancing with Inertia of a Wearable Robotic Appendage," *2020 IEEE/RSJ International Conference on Intelligent Robots and Systems (IROS)*, pp. 4077–4082, doi: 10.1109/IROS45743.2020.9341323.

[17] Chang-Siu, E., Libby, T., Tomizuka, M., and Full, R. J., 2011, "A lizard-inspired active tail enables rapid maneuvers and dynamic stabilization in a terrestrial robot," *2011 IEEE/RSJ International Conference on Intelligent Robots and Systems*, pp. 1887–1894, doi: 10.1109/IROS.2011.6094658.

[18] Briggs, R., Lee, J., Haberland, M., and Kim, S., 2012, "Tails in biomimetic design: Analysis, simulation, and experiment," *2012 IEEE/RSJ International Conference on Intelligent Robots and Systems*, pp. 1473–1480, doi: 10.1109/IROS.2012.6386240.

[19] Patel, A. and Braae, M., 2013, "Rapid turning at high-speed: Inspirations from the cheetah's tail," *2013 IEEE/RSJ International Conference on Intelligent Robots and Systems*, pp. 5506–5511, doi: 10.1109/IROS.2013.6697154.

[20] Abeywardena, S., Anwar, E., Miller, S., and Farkhatdinov, I., 2022, "Human balance augmentation via a supernumerary robotic tail," *2022 44th Annual International Conference of the IEEE Engineering in Medicine & Biology Society (EMBC)*, pp. 2878–2881, doi: 10.1109/EMBC48229.2022.9871317.

[21] Peterka, R. J., 2000, "Postural control model interpretation of stabilogram diffusion analysis," Biological Cybernetics, **82**, pp. 335–343.

[22] Gage, W. H., Winter, D. A., Frank, J. S., and Adkin, A. L., 2004, "Kinematic and kinetic validity of the inverted pendulum model in quiet standing," Gait and Posture, **19**(2), pp. 124–132.

[23] Morasso, P., Cherif, A., and Zenzeri, J., 2019, "Quiet standing: The Single Inverted Pendulum model is not so bad after all," PLOS ONE, **14**(3), pp. 1–20.

[24] National Aeronautics and Space Administration, 2000, "Anthropometry and Biomechanics," https://msis.jsc.nasa.gov/sections/section03.htm#_3.3_ANTHROPOMETRIC_AND.

[25] Angeles, J., 2007, *Fundamentals of Robotic Mechanical Systems: Theory, Methods and Algorithms*, 3rd ed., Springer.

[26] Abeywardena, S. and Chen, C., 2017, "Inverse dynamic modelling of a three-legged six-degree-of-freedom parallel mechanism," Multibody System Dynamics, **41**(1), pp. 1–24.

[27] Asai, Y., Tasaka, Y., Nomura, K., Nomura, T., Casadio, M., and Morasso, P., 2009, "A Model of Postural Control in Quiet Standing: Robust Compensation of Delay-Induced Instability Using Intermittent Activation of Feedback Control," PLOS ONE, **4**(7), pp. 1–14.

[28] Azad, M., Babic, J., and Mistry, M., 2019, "Effects of the weighting matrix on dynamic manipulability of robots," Autonomous Robots, **43**, pp. 1867–1879.

[29] Meuleman, J. H., van Asseldonk, E. H., and van der Kooij, H., 2013, "The effect of directional inertias added to pelvis and ankle on gait," Journal of NeuroEngineering and Rehabilitation, **10**, p. 40.

[30] Moraux, A., Canal, A., Ollivier, G., Ledoux, I., Doppler, V., Payan, C., and Hogrel, J.-Y., 2013, "Ankle dorsi- and plantar-flexion torques measured by dynamometry in healthy subjects from 5 to 80 years," BMC Musculoskeletal Disorders, **14**(1), p. 104.

[31] Tits, A. and Yang, Y., 1996, "Globally convergent algorithms for robust pole assignment by state feedback," IEEE Transactions on Automatic Control, **41**(10), pp. 1432–1452.

[32] Wang, S., Wang, L., Meijneke, C., van Asseldonk, E., Hoellinger, T., Cheron, G., Ivanenko, Y., La Scaleia, V., Sylos-Labini, F., Molinari, M., Tamburella, F., Pisotta, I., Thorsteinsson, F., Ilzkovitz, M., Gancet, J., Nevatia, Y., Hauffe, R., Zanow, F., and van der Kooij, H., 2015, "Design and Control of the MINDWALKER Exoskeleton," IEEE Transactions on Neural Systems and Rehabilitation Engineering, **23**(2), pp. 277–286.

[33] Abeywardena, S. and Farkhatdinov, I., in press, "Towards enhanced stability of human stance with a supernumerary robotic tail," IEEE Robotics and Automation Letters.

Supplemental Material: Dynamic Models and Stationary Points

1 DYNAMIC MODEL

For the one-dof SRTs, the generalised inertia, coriolis, gravity and Jacobian matrices are respectively in the form

$$\mathbf{M}_q = \begin{bmatrix} m_{11} & m_{12} \\ m_{12} & m_{22} \end{bmatrix} \qquad \mathbf{C}_q = \begin{bmatrix} \eta_{11} & \eta_{12} \\ \eta_{21} & \eta_{22} \end{bmatrix}$$
$$\mathbf{G}_q = \begin{bmatrix} g_{11} \\ g_{21} \end{bmatrix} \qquad \mathbf{J} = \frac{1}{m_s} \begin{bmatrix} j_{11} & j_{12} \\ j_{21} & j_{22} \end{bmatrix} \quad (1)$$

The terms for one-dof tails are,

Linear Counter Mass (LCM)

$$\begin{aligned}
m_{11} &= m\left({\beta_1}^2 + {\beta_2}^2\right) + I_s + m_c\left(h_t^2 + d_c^2\right) \\
m_{12} &= m_c h_t \\
m_{22} &= m_c \\
\eta_{11} &= 2m_c d_c \dot{d}_c \\
\eta_{12} &= 0 \\
\eta_{21} &= -m_c d_c \dot{q}_1 \\
\eta_{22} &= 0 \\
g_{11} &= -\left(m\beta_1 + m_c h_t\right) s_1 + \left(-m\beta_2 + m_c d_c\right) c_1 \\
g_{21} &= m_c s_1 \\
j_{11} &= -m\left(\beta_1 c_1 - \beta_2 s_1\right) \\
&\quad - m_c\left(h_t c_1 + d_c s_1\right) \\
j_{12} &= -m_c c_1 \\
j_{21} &= m\left(\beta_1 s_1 + \beta_2 c_1\right) \\
&\quad - m_c\left(d_c c_1 - h_t s_1\right) \\
j_{22} &= m_c s_1 \\
m &= m_b + m_a + m_l + m_t \\
m_s &= m + m_c \\
\beta_1 &= \frac{m_b h_b + m_a h_a + m_l h_l + m_t h_t}{m} \\
\beta_2 &= \frac{m_a h_a + m_l h_l - \frac{1}{2} m_t l_t}{m}
\end{aligned}$$

Reaction Wheel (RW)

$$\begin{aligned}
m_{11} &= m\left(\beta_1^2 + \beta_2^2\right) + I_s + I_w + m_w\left(h_t^2 + l_t^2\right) \\
m_{12} &= I_w \\
m_{22} &= I_w \\
\eta_{11} &= 0 \\
\eta_{12} &= 0 \\
\eta_{21} &= 0 \\
\eta_{22} &= 0 \\
g_{11} &= -m\left(\beta_1 s_1 - \beta_2 c_1\right) + m_w\left(l_t c_1 - h_t s_1\right) \\
g_{21} &= 0 \\
j_{11} &= -m\left(\beta_1 c_1 - \beta_2 s_1\right) - m_w\left(h_t c_1 + l_t s_1\right) \\
j_{12} &= 0 \\
j_{21} &= m\left(\beta_1 s_1 + \beta_2 c_1\right) + m_w\left(h_t s_1 - l_t c_1\right) \\
j_{22} &= 0 \\
m &= m_b + m_a + m_+ m_t l \\
m_s &= m + m_w \\
\beta_1 &= \frac{m_b h_b + m_a h_a + m_l h_l + m_t h_t}{m} \\
\beta_2 &= \frac{m_a h_a + m_l h_l - \frac{1}{2} m_t l_t}{m}
\end{aligned}$$

Arc

$$\begin{aligned}
m_{11} &= m\left({\beta_1}^2 + {\beta_2}^2\right) + I_s + I_t + m_t\left(h_t^2 + l_t^2 + 2 l_t h_t c_2\right) \\
m_{12} &= m_t {l_t}^2 + m_t l_t h_t c_2 + I_t \\
m_{22} &= m_t {l_t}^2 + I_t \\
\eta_{11} &= -2 m_t l_t h_t s_2 \dot{q}_2 \\
\eta_{12} &= -m_t l_t h_t s_2 \dot{q}_2 \\
\eta_{21} &= m_t l_t h_t s_2 \dot{q}_1 \\
\eta_{22} &= 0
\end{aligned}$$

$$
\begin{aligned}
g_{11} &= -\left(m\beta_1 + m_t h_t\right) s_1 \\
&\quad - m\beta_2 c_1 - m_t l_t s_{1-2} \\
g_{21} &= m_t l_t s_{1-2} \\
j_{11} &= -m\left(\beta_1 c_1 - \beta_2 s_1\right) - m_t\left(h_t c_1 + l_t c_{1-2}\right) \\
j_{12} &= -m_t l_t c_{1-2} \\
j_{21} &= m\left(\beta_1 s_1 + \beta_2 c_1\right) + m_t\left(h_t s_1 + l_t s_{1-2}\right) \\
j_{22} &= m_t l_t s_{1-2} \\
m &= m_b + m_a + m_l \\
m_s &= m + m_t \\
\beta_1 &= \frac{m_b h_b + m_a h_a + m_l h_l}{m} \\
\beta_2 &= \frac{m_a l_a + m_l l_l}{m}
\end{aligned}
$$

For the two-dof SRTs, the generalised inertia, coriolis, gravity and Jacobian matrices are respectively in the form

$$
\mathbf{M}_q = \begin{bmatrix} m_{11} & m_{12} & m_{13} \\ m_{12} & m_{22} & m_{23} \\ m_{13} & m_{23} & m_{33} \end{bmatrix} \qquad \mathbf{C}_q = \begin{bmatrix} \eta_{11} & \eta_{12} & \eta_{13} \\ \eta_{21} & \eta_{22} & \eta_{23} \\ \eta_{31} & \eta_{32} & \eta_{33} \end{bmatrix}
$$

$$
\mathbf{G}_q = \begin{bmatrix} g_{11} \\ g_{21} \\ g_{31} \end{bmatrix} \qquad \mathbf{J} = \frac{1}{m_s} \begin{bmatrix} j_{11} & j_{12} & j_{13} \\ j_{21} & j_{22} & j_{23} \end{bmatrix}
$$

The terms for the *Planar-Serial Two-dof (PS2)* tail are

$$
\begin{aligned}
m_{11} &= I_b + I_{t1} + I_{t2} + \left({\beta_1}^2 + {\beta_2}^2\right) m + \left(m_{t1} + m_{t2}\right) {h_t}^2 \\
&\quad + \left(\frac{1}{4} m_{t1} + m_{t2}\right) {l_{t1}}^2 + \frac{1}{4} m_{t2} {l_{t2}}^2 + m_{t2} h_t l_{t2} c_{23} \\
&\quad + m_{t1} h_t l_{t1} c_2 + 2 m_{t2} h_t l_{t1} c_2 + m_{t2} l_{t1} l_{t2} c_3 \\
m_{12} &= -I_{t1} - I_{t2} - \left(\frac{1}{4} m_{t1} - m_{t2}\right) {l_{t1}}^2 - \frac{1}{4} m_{t2} {l_{t2}}^2 \\
&\quad - \frac{1}{2} m_{t2} h_t l_{t2} c_{23} - \frac{1}{2} m_{t1} h_t l_{t1} c_2 - m_{t2} h_t l_{t1} c_2 \\
&\quad - m_{t2} l_{t1} l_{t2} c_3 \\
m_{13} &= -I_{t2} - \frac{1}{4} m_{t2} {l_{t2}}^2 - \frac{1}{2} m_{t2} h_t l_{t2} c_{23} - \frac{1}{2} m_{t2} l_{t1} l_{t2} c_3 \\
m_{22} &= I_{t1} + I_{t2} + \left(\frac{1}{4} m_{t1} + m + t2\right) {l_{t1}}^2 + \frac{1}{4} m_{t2} {l_{t2}}^2 \\
&\quad + m_{t2} l_{t1} l_{t2} c_3 \\
m_{23} &= \frac{1}{4} m_{t2} {l_{t2}}^2 + \frac{1}{2} m_{t2} l_{t1} l_{t2} c_3 + I_{t2} \\
m_{33} &= \frac{1}{4} m_{t2} {l_{t2}}^2 + I_{t2} \\
\eta_{11} &= \dot{q}_2\left(-m_{t1} h_t l_{t1} s_2 + m_{t2}\left(-2 h_t l_{t1} s_2 - m_{t2} h_t l_{t2} s_{23}\right)\right) \\
&\quad + \dot{q}_3 m_{t2}\left(-l_{t1} l_{t2} s_3 - h_t l_{t2} s_{23}\right) \\
\eta_{12} &= \dot{q}_2\left(\frac{1}{2}\left(m_{t1} h_t l_{t1} s_2\right) + m_{t2} h_t\left(l_{t2} s_{23} + l_{t1} s_2\right)\right) \\
&\quad + \dot{q}_3 m_{t2}\left(l_{t1} l_{t2} s_3 + h_t l_{t2} s_{23}\right) \\
\eta_{13} &= \frac{1}{2} \dot{q}_3 m_{t2} l_{t2}\left(h_t s_{23} + l_{t1} s_3\right) \\
\eta_{21} &= \dot{q}_1\left(\frac{1}{2}\left(m_{t2} h_t l_{t2} s_{23} + m_{t1} h_t l_{t1} s_2\right) + m_{t2} h_t l_{t1} s_2\right) \\
&\quad + \dot{q}_3 m_{t2} l_{t1} l_{t2} s_3 \\
\eta_{22} &= -\dot{q}_3 m_{t2} l_{t1} l_{t2} s_3 \\
\eta_{23} &= -\frac{1}{2} \dot{q}_3 m_{t2} l_{t1} l_{t2} s_3 \\
\eta_{31} &= \frac{1}{2} \dot{q}_1 m_{t2} l_{t2}\left(h_t s_{23} + l_{t1} s_3\right) - \dot{q}_2 m_{t2} l_{t1} l_{t2} s_3 \\
\eta_{32} &= \frac{1}{2} \dot{q}_2 m_{t2} l_{t1} l_{t2} s_3 \\
\eta_{33} &= 0 \\
g_{11} &= -m\left(\beta_1 s_1 + \beta_2 c_1\right) - m_{t1}\left(h_t s_1 + \frac{1}{2} l_{t1} s_{1-2}\right) \\
&\quad + m_{t2}\left(-h_t s_1 - l_{t1} s_{1-2} + \frac{1}{2} l_{t2} s_{23-1}\right) \\
g_{21} &= \frac{1}{2} m_{t1} l_{t1} s_{1-2} + m_{t2}\left(l_{t1} s_{1-2} - \frac{1}{2} l_{t2} s_{23-1}\right) \\
g_{31} &= -\frac{1}{2} m_{t2} l_{t2} s_{23-1} \\
j_{11} &= \frac{1}{2}\left(m\left(2\beta_1 c_1 - 2\beta_2 s_1\right) + m_{t1}\left(2 h_t c_1 + l_{t1} c_{1-2}\right)\right. \\
&\quad \left. + m_{t2}\left(2 h_t c_1 + 2 l_{t1} c_{1-2} + l_{t2} c_{23-1}\right)\right) \\
j_{12} &= -\frac{1}{2}\left(m_{t1} l_{t1} c_{1-2} + m_{t2}\left(2 l_{t1} c_{1-2} + l_{t2} c_{23-1}\right)\right) \\
j_{13} &= -\frac{1}{2} m_{t2} l_{t2} c_{23-1} \\
j_{21} &= -\frac{1}{2}\left(m\left(2\beta_2 c_1 + 2\beta_1 s_1\right) + m_{t1}\left(2 h_t s_1 + l_{t1} s_{1-2}\right)\right. \\
&\quad \left. + m_{t2}\left(2 h_t s_1 + 2 l_{t1} s_{1-2} - l_{t2} s_{23-1}\right)\right) \\
j_{22} &= \frac{1}{2}\left(l_{t1} m_{t1} s_{1-2} + m_{t2}\left(2 l_{t1} s_{1-2} - l_{t2} s_{23-1}\right)\right) \\
j_{23} &= -\frac{1}{2} m_{t2} l_{t2} s_{23-1} \\
m &= m_b + m_a + m_l \\
m_s &= m + m_{t1} + m_{t2} \\
\beta_1 &= \frac{m_b h_b + m_a h_a + m_l h_l}{m}
\end{aligned}
$$

$$\beta_2 = \frac{m_a l_a + m_l l_l}{m}$$

2 FIVE BAR SRT DYNAMICS

Due to the closed loop kinematic structure and passive joints of the five-bar SRT, a symbolic form of the dynamic model is difficult to obtain. To derive the dynamics of this system, the natural-orthogonal complement was utilised. In this appendix, the relevant matrices of the NOC method are provided. For an overview of the algorithm itself, the reader is directed to [1] and [2].

The NOC method is reliant on deriving the twist matrix $\mathbf{S}$ which is the orthogonal complement to the kinematic constraints. This requires determining the twists $\mathbf{t}_i$ of all the bodies of the system under study, in terms of all the joints—active and passive. These twists can be derived using elementary techniques used for serial mechanisms such as recursion and differentiation. Hence, the twist of each body i can be written in the form

$$^{i}\mathbf{t}_i = {}^{i}\mathbf{Y}_i \dot{\mathbf{q}} \tag{2}$$

where $\dot{\mathbf{q}}$ is the vector of active $(\dot{\mathbf{q}}_a)$ and passive $(\dot{\mathbf{q}}_p)$ joint rates. For the FB SRT system, $\dot{\mathbf{q}}$ is of dimension 5×1.

Choosing the base frame $\mathcal{F}_0$ as a common frame of reference; concatenation of Eq. (2) for the rigid bodies of the FB tail system yields

$$\begin{bmatrix} {}^{0}\mathbf{t}_1 \\ {}^{0}\mathbf{t}_{2a} \\ {}^{0}\mathbf{t}_{2b} \\ {}^{0}\mathbf{t}_{3a} \\ {}^{0}\mathbf{t}_{3b} \end{bmatrix} = \begin{bmatrix} {}^{0}\mathbf{Y}_1 \\ {}^{0}\mathbf{Y}_{2a} \\ {}^{0}\mathbf{Y}_{2b} \\ {}^{0}\mathbf{Y}_{3a} \\ {}^{0}\mathbf{Y}_{3b} \end{bmatrix} \begin{bmatrix} \dot{q}_1 \\ \dot{q}_{2a} \\ \dot{q}_{2b} \\ \dot{q}_{3a} \\ \dot{q}_{3b} \end{bmatrix}$$
$$\mathbf{t}_M = \mathbf{Y}\dot{\mathbf{q}} \tag{3}$$

where $\mathbf{Y}$ is a 30×5 twist matrix. Clearly, the individual $\mathbf{Y}_i$ are the Jacobians for each individual rigid body with respect to all the joint rates of the system.

The NOC method, however, requires the twists to be expressed in terms of the active joints only. To eliminate the passive joint rates, the manipulator Jacobian $\mathbf{J}_M$ defined at a common point such as the global CoM can be utilised. For the Human-FB tail system, the twist of this point can be derived in the base frame $\mathcal{F}_0$ in form

$${}^{0}\mathbf{t}_{cm} = {}^{0}\mathbf{J}_{cm}\dot{\mathbf{q}} \tag{4}$$

where ${}^{0}\mathbf{J}_{cm}$ is a 2×5 matrix in terms of the active and passive joints of the system, and termed as the full manipulator Jacobian.

Inverting this equation, the joint rates can be determined

$$\dot{\mathbf{q}} = {}^{0}\mathbf{J}^{\dagger}_{cm}\,{}^{0}\mathbf{t}_{cm} \tag{5}$$

where ${}^{0}\mathbf{J}^{\dagger}_{cm}$ is a pseudo-inverse.

For the five-bar SRT system, the joint rate vector is of form $\dot{\mathbf{q}} = [\dot{q}_1, \dot{q}_{2a}, \dot{q}_{2b}, \dot{q}_{3a}, \dot{q}_{3b}]^T$, where the passive joint rates are $\dot{q}_{2b}$ and $\dot{q}_{3b}$. As such, from Eq. (5), the following two matrices can be defined

$${}^{0}\mathbf{J}^{\dagger}_{M} = {}^{0}\mathbf{J}^{\dagger}_{cm}\left([1,2,4],:\right) \tag{6}$$
$${}^{0}\mathbf{J}^{\dagger}_{P} = {}^{0}\mathbf{J}^{\dagger}_{cm}\left([3,5],:\right) \tag{7}$$

where ${}^{0}\mathbf{J}^{\dagger}_{M}$ is a 3×2 reduced Jacobian matrix also termed the manipulator Jacobian as it only considers the active joint rates, i.e

$$\dot{\mathbf{q}}_a = {}^{0}\mathbf{J}^{\dagger}_{M}\,{}^{0}\mathbf{t}_{cm} \tag{8}$$

Further, ${}^{0}\mathbf{J}^{\dagger}_{P}$ is a 2×2 Jacobian matrix termed the passive joint Jacobian, i.e.

$$\dot{\mathbf{q}}_p = {}^{0}\mathbf{J}^{\dagger}_{P}\,{}^{0}\mathbf{t}_{cm} \tag{9}$$

Rearranging Eq. (8) for ${}^{0}\mathbf{t}_{cm}$ and substituting into Eq. (9), the passive joint rates can be found in terms of the active rates, i.e.

$$\dot{\mathbf{q}}_p = {}^{0}\mathbf{J}^{\dagger}_{P}\,{}^{0}\mathbf{J}_M\dot{\mathbf{q}}_a \tag{10}$$

Substituting Eq. (10) into Eq. (3), the twist relationship becomes

$$\mathbf{t}_M = \left(\mathbf{Y}\left(:,[1,2,4]\right) + \mathbf{Y}\left(:,[3,5]\right){}^{0}\mathbf{J}^{\dagger}_{P}\,{}^{0}\mathbf{J}_M\right)\dot{\mathbf{q}}_a$$
$$\mathbf{t}_M = \mathbf{S}\dot{\mathbf{q}}_a \tag{11}$$

where $\mathbf{S}$ is the 30×3 twist matrix of the system, solely with respect to the active joint rates.

With the twist matrix derived, the NOC method proceeds by determining the individual wrenches of the rigid bodies using the Newton-Euler equation, i.e. expressed at

the frame of origin, the wrench $\mathbf{w}_i$ is

$$
\begin{aligned}
{}^i\mathbf{w}_i &= \begin{bmatrix} m_i\mathbf{1}_3 & -{}^i\hat{\boldsymbol{\eta}}_i \\ {}^i\hat{\boldsymbol{\eta}}_i & {}^i\mathbf{I}_i \end{bmatrix} {}^i\dot{\mathbf{t}}_i + \begin{bmatrix} \mathbf{0}_{3\times3} & -{}^i\hat{\boldsymbol{\omega}}_i {}^i\hat{\boldsymbol{\eta}}_i \\ \mathbf{0}_{3\times3} & {}^i\hat{\boldsymbol{\omega}}_i {}^i\mathbf{I}_i \end{bmatrix} {}^i\mathbf{t}_i \\
&\quad - \begin{bmatrix} m_i\mathbf{1}_3 \\ {}^i\hat{\boldsymbol{\eta}}_i \end{bmatrix} {}^i\mathbf{g} \\
&= \mathbf{M}_i {}^i\dot{\mathbf{t}}_i + \mathbf{W}_i {}^i\mathbf{t}_i + \mathbf{G}_i
\end{aligned} \tag{12}
$$

where the following notation is utilised,

${}^i\mathbf{w}_i = \left[{}^i\mathbf{f}_i^T \ {}^i\mathbf{n}_i^T \right]^T$ is the wrench of the i^{th} body acting at the origin of $\mathcal{F}_i$;
${}^i\mathbf{v}_i$ and ${}^i\boldsymbol{\omega}_i$ are the linear and angular velocities of the i^{th} body with ${}^i\dot{\mathbf{v}}_i$ and ${}^i\dot{\boldsymbol{\omega}}_i$ the associated linear and angular accelerations in $\mathcal{F}_i$;
${}^i\mathbf{g}$ is the 3×1 vector of the acceleration due to gravity in $\mathcal{F}_i$;
m_i is the mass of the i^{th} body;
${}^i\mathbf{I}_i$ is the 3×3 inertia matrix of the i^{th} body in $\mathcal{F}_i$, with ${}^i\mathbf{I}_i = \begin{bmatrix} XX_i & XY_i & XZ_i \\ XY_i & YY_i & YZ_i \\ XZ_i & YZ_i & ZZ_i \end{bmatrix}$;
${}^i\boldsymbol{\eta}_i = m_i {}^i\mathbf{s}_i = [MX_i, MY_i, MZ_i]^T$ are the first moments around the origin of $\mathcal{F}_i$ with ${}^i\hat{\boldsymbol{\eta}}_i$ being the associated skew symmetric matrix;
${}^i\mathbf{s}_i$ is the 3×1 vector from the origin of $\mathcal{F}_i$ to the centre of mass of the i^{th} body; and
$\mathbf{1}_3$ is the 3×3 identity matrix.

In the case that a frame of reference different to rigid body i's native frame $\mathcal{F}_i$ is utilised, such as base frame $\mathcal{F}_0$, similarity transforms must be applied to ${}^i\hat{\boldsymbol{\eta}}_i$ and ${}^i\mathbf{I}_i$, i.e.

$$
{}^0\mathbf{I}_i = {}^0\mathbf{Q}_i {}^i\mathbf{I}_i {}^0\mathbf{Q}_i^T \qquad {}^0\hat{\boldsymbol{\eta}}_i = {}^0\mathbf{Q}_i {}^i\hat{\boldsymbol{\eta}}_i {}^0\mathbf{Q}_i^T
$$

where ${}^0\mathbf{Q}_i$ is a rotation matrix.

For the five-bar SRT, the wrenches of the individual rigid bodies are derived with respect to $\mathcal{F}_0$. The individual matrices of Eq. (12) are concatenated to form $\mathbf{M} = \text{blkdiag}\left([\mathbf{M}_1, \mathbf{M}_{2a}, \mathbf{M}_{2b}, \mathbf{M}_{3a}, \mathbf{M}_{3b}]\right)$ and $\mathbf{W} = \text{blkdiag}\left([\mathbf{W}_1, \mathbf{W}_{2a}, \mathbf{W}_{2b}, \mathbf{W}_{3a}, \mathbf{W}_{3b}]\right)$ which are 30×30 generalised matrices, and $\mathbf{G} = \text{diag}\left([\mathbf{G}_1, \mathbf{G}_{2a}, \mathbf{G}_{2b}, \mathbf{G}_{3a}, \mathbf{G}_{3b}]\right)$, a 30×1 matrix.

The inverse dynamic model of the Human-FB tail system in terms of solely the active joint rates can then be derived, i.e.

$$
\mathbf{M}_q = \mathbf{S}^T\mathbf{M}\mathbf{S}
$$

$$
\mathbf{C}_q = \mathbf{S}^T\left(\mathbf{M}\dot{\mathbf{S}} + \mathbf{W}\mathbf{S}\right)
$$

$$
\boldsymbol{G}_q = \mathbf{S}^T\mathbf{G}
$$

3 STATIONARY POINTS FOR TWO-DOF SRTS

For the two-dof SRTs, the x co-ordinate of the tail's CoM for static balance is defined by the equation

$$
{}^0s_x = -\frac{m_a l_a + m_l l_l}{m_t} \tag{13}
$$

However, due to the redundant dof, the corresponding y co-ordinate cannot be uniquely determined. In this appendix, the algorithm used to find all feasible stationary points for the PS2 and five-bar SRTs are described.

3.1 Planar Serial Two-dof Tail

The location of the CoM of the PS2 tail is given by

$$
{}^0\mathbf{s}_{PS2} = \begin{bmatrix} {}^0s_x \\ {}^0s_y \\ 0 \end{bmatrix} = \frac{m_{t1} {}^0\mathbf{s}_{t1} + m_{t2} {}^0\mathbf{s}_{t2}}{m_{t1} + m_{t2}} \tag{14}
$$

As the stationary point is found in upright stance, the ${}^0\mathbf{s}_{PS2}$ can be transformed into a frame of the tail, i.e. imagine there is an intermediary fixed base frame $\mathcal{F}_{20}$ located at the origin of $\mathcal{F}_2$. Then, in the pose corresponding to upright stance

$$
{}^{20}\mathbf{s}_{PS2} = {}^{20}\mathbf{T}_0 \begin{bmatrix} {}^0\mathbf{s}_{PS2} \\ 1 \end{bmatrix} \qquad \begin{bmatrix} {}^{20}s_x \\ {}^{20}s_y \\ 0 \end{bmatrix} = \begin{bmatrix} {}^0s_y \\ -{}^0s_x \\ 0 \end{bmatrix} \tag{15}
$$

Hence, in the transformed state, the task is to find ${}^{20}s_x$. Without loss of generality, from here on, let $x_{cm} = {}^{20}s_x$ and $y_{cm} = {}^{20}s_y$.

For the two links of the PS2 tail, the CoM vectors in the frame $\mathcal{F}_i$ are

$$
{}^2\mathbf{s}_2 = \begin{bmatrix} \frac{l_{t1}}{2} \\ 0 \\ 0 \end{bmatrix} \qquad {}^3\mathbf{s}_3 = \begin{bmatrix} \frac{l_{t2}}{2} \\ 0 \\ 0 \end{bmatrix} \tag{16}
$$

Thus, the CoM of the tail in $\mathcal{F}_{20}$ can be expressed as

$$
x_{cm} = \frac{m_{t1} l_{t1} c_2 + m_{t2}\left(2l_{t1}c_2 + l_{t2}c_{23}\right)}{2m_t} \tag{17a}
$$

$$y_{cm} = \frac{m_{t1} l_{t1} s_2 + m_{t2} \left(2 l_{t1} s_2 + l_{t2} s_{23}\right)}{2 m_t} \tag{17b}$$

where $m_t = m_{t1} + m_{t2}$.

Squaring and adding the two equations of Eq. (17), yields

$$\left(a_1 x_{cm} - a_2 c_2\right)^2 + \left(a_1 y_{cm} - a_2 s_2\right)^2 = {a_3}^2 \tag{18}$$

where $a_1 = 2m_t$, $a_2 = \left(m_{t1} + 2m_{t2}\right) l_{t1}$ and $a_3 = m_{t2} l_{t2}$.

Equation (18) is in terms of two unknowns; x_{cm} and q_2. As the extra-dof of the tail adds redundancy to the system, a range of values can be set for q_2 and the associated value for x_{cm} determined. Hence, as the tail should not interfere with the body, q_2 can only range from 0 to π. Thus, Eq. (18) can be written as a quadratic equation in x_{cm},

$$A_2 {x_{cm}}^2 + A_1 x_{cm} + A_0 = 0 \tag{19}$$

where $A_2 = {a_1}^2$, $A_1 = -2 a_1 a_2 c_2$ and $A_0 = {a_1}^2 {y_{cm}}^2 + {a_2}^2 - {a_3}^2 - 2 a_1 a_2 y_{cm} s_2$.

Hence, the solution of x_{cm} is readily derived from the quadratic equation,

$$x_{cm} = \frac{-A_1 \pm \sqrt{{A_1}^2 - 4 A_0 A_2}}{2 A_2} \tag{20}$$

i.e. for each value of q_2, there are two potential values of x_{cm}.

However, for the stationary point to be feasible, the solution to Eq. (20) must be real. That is, the discriminant is non-negative i.e.

$${A_1}^2 - 4 A_0 A_2 \geq 0$$

Further, all solutions to x_{cm} must be above the ground. Due to the frame transformation, this corresponds to the condition

$$x_{cm} > -h_t$$

Hence, all valid locations of the tail's CoM have been found. The final task is to find the associated joint value of q_3 to position the CoM at this location, i.e. from Eq. (17)

$$q_3 = \arctan\left(\frac{a_1 y_{cm} - a_2 s_2}{a_1 x_{cm} - a_2 c_2}\right) - q_2 \tag{21}$$

A suitable metric can then be utilised to select which stationary point is used.

3.2 Five-Bar Tail

The location of the CoM of the FB tail is given by

$${}^0\mathbf{s}_{FB} = \frac{m_{2a}\,{}^0\mathbf{s}_{2a} + m_{2b}\,{}^0\mathbf{s}_{2b} + m_{3a}\,{}^0\mathbf{s}_{3a} + m_{3b}\,{}^0\mathbf{s}_{3b}}{m_{2a} + m_{2b} + m_{3a} + m_{3b}} \tag{22}$$

As with the PS2, the CoM can be transformed from base frame to an intermediate base frame located at the origin of $\mathcal{F}_{2a,0}$. In this frame, the CoM of the tail has the same transformation as Eq. (15). Hence, let $x_{cm} = {}^{2a,0}s_x = {}^0 s_y$ and $y_{cm} = {}^{2a,0}s_y = -{}^0 s_x$.

For the five-bar tail, the CoM of the segments of the limbs in the frame F_i are

$${}^{ia}\mathbf{s}_{ia} = \begin{bmatrix} \frac{l_{ia}}{2} \\ 0 \\ 0 \end{bmatrix} \qquad {}^{ib}\mathbf{s}_{ib} = \begin{bmatrix} \frac{l_{ib}}{2} \\ 0 \\ 0 \end{bmatrix} \tag{23}$$

for $i = 2, 3$

As there are two PS2 limbs which connect at the free end, the tail CoM is determined by the location of the two limbs, i.e.

$$x_{cm} = \frac{m_2 x_{c2} + m_3 x_{c3}}{2 m_t} \tag{24a}$$

$$y_{cm} = \frac{m_2 y_{c2} + m_3 y_{c3}}{2 m_t} \tag{24b}$$

where $m_t = m_2 + m_3$, $m_i = m_{ia} + m_{ib}$ for $i = 2, 3$ and

$$x_{ci} = \frac{\left(m_{ia} + 2 m_{ib}\right) l_{ia} c_{ia} + m_{ib} l_{ib} c_{iaib}}{2 m_i} + r_i \tag{25a}$$

$$y_{ci} = \frac{\left(m_{ia} + 2 m_{ib}\right) l_{ia} s_{ia} + m_{ib} l_{ib} s_{iaib}}{2 m_i} \tag{25b}$$

where $r_2 = 0$ and $r_3 = d_3$.

Squaring the two equations of Eq. (25) and adding

results in

$$(x_{ci} - a_i c_{ia} - r_i)^2 + (y_{ci} - a_i s_{ia})^2 = {b_i}^2 \quad (26)$$

where $a_i = \frac{(m_{ia}+2m_{ib})l_{ia}}{2m_i}$ and $b_i = \frac{m_{ib}l_{ib}}{2m_i}$

Consider Eq. (24b). In this, y_{cm} is known; however it is dependent on the location of y_{c2} and y_{c3}. Given that the tail can not interfere with the body, let the y-coordinate y_{c2} range from its minimal value of 0 to its maximum value of $l_{2a} + l_{2b}$. Hence, y_{c3} is expressed as

$$y_{c3} = \frac{m_t y_{cm} - m_2 y_{c2}}{m_3} \quad (27)$$

Therefore, having chosen a value of y_{c2}, it and y_{c3} are known. Thus, Eq. (26) are two decoupled equations of two unknowns each; x_{ci} and q_{ia} for $i = 2, 3$. Expanding out this equation, it can be factored as

$$2a_i (r_i - x_{ci}) c_{ia} - 2a_i y_{ci} s_{ia} + {x_{ci}}^2 + k_i = 0 \quad (28)$$

where $k_i = {a_i}^2 - {b_i}^2 + {r_i}^2 + {y_{ci}}^2$.

Utilising the trigonometric substitutions $c_{ia} = \frac{1-{u_{ia}}^2}{1+{u_{ia}}^2}$, $s_{ia} = \frac{2u_{ia}}{1+{u_{ia}}^2}$ and $u_{ia} = \tan\left(\frac{q_{2a}}{2}\right)$; Eq. (29) becomes quadratic in u_{ia}

$$A_2 {u_{ia}}^2 + A_1 u_{ia} + A_0 = 0 \quad (29)$$

where $A_2 = {x_{ci}}^2 + 2a_i (x_{ci} - r_i) + k_i$, $A_1 = -4a_i y_{ci}$ and $A_0 = {x_{ci}}^2 - 2a_i (x_{ci} - r_i) + k_i$.

Clearly, the coefficients of Eq. (29) are functions of x_{ci}. Let x_{ci} be arbitrarily set to determine all potential solutions, i.e. taking into account physical constraints and frame transformation, the feasible region is $x_{ci} \geq -h_t$ [1]. For a potential feasible solution to exist, however, the following condition based on the discriminant must be met for the chosen values of x_{ci}

$${A_1}^2 - 4A_0 A_2 \geq 0$$

Whilst satisfaction of the above condition may guarantee that the CoM of limb i can be positioned at (x_{ci}, y_{ci}), it does not guarantee that the CoM of the tail can be positioned at y_{cm}, nor does it guarantee a feasible configuration (x, y) of the linkage can be assembled as it requires co-ordination with the other limb. Hence, rather than solving for the associated variable u_{ia}, the pair (x_{ci}, y_{ci}) is deemed viable for limb i. To determine if it leads to a viable y_{cm} and configuration of the mechanism (x, y), all the combinations of feasible (x_{c2}, y_{c2}) and (x_{c3}, y_{c3}) need to be checked. That is, for each potential combination of pairs (x_{c2}, y_{c2}) and (x_{c3}, y_{c3}), only the combinations that satisfy

$$y_c = \frac{y_{c2} + y_{c3}}{2}$$

are deemed as potential stationary configurations of the tail.

With the feasible combinations of $(x_{c2}, y_{c2}, x_{c3}, y_{c3})$ determined, it needs to be checked if they lead to an attainable configuration of the common end point of the five bar linkage. The co-ordinates of this point are calculated from

$$x = l_{ia} c_{ia} + l_{ib} c_{iaib} + r_i \quad (30a)$$
$$y = l_{ia} s_{ia} + l_{ib} s_{iaib} \quad (30b)$$

Rearranging Eq. (30), the $q_{ia} + q_{ib}$ terms can be isolated and substituted into Eq. (25) to obtain

$$x - \frac{2m_i x_{ci}}{m_{ib}} + \frac{(2m_{ia} + m_{ib}) r_i}{m_{ib}} = -\frac{m_i l_{ia} c_{ia}}{m_{ib}} \quad (31a)$$
$$y - \frac{2m_i y_{ci}}{m_{ib}} = -\frac{m_i l_{ia} s_{ia}}{m_{ib}} \quad (31b)$$

Squaring the constituent equations of Eq. (31) and adding, yields

$$(x - a_{xi})^2 + (y - a_{yi})^2 = {\rho_i}^2 \quad (32)$$

where $a_{xi} = \frac{2m_i x_{ci}}{m_{ib}} - \frac{(2m_{ia}+m_{ib})r_i}{m_{ib}}$, $a_{yi} = \frac{2m_i y_{ci}}{m_{ib}}$ and $\rho_i = \frac{m_i l_{ia}}{m_{ib}}$. These are simply equations of two circles for $i = 2, 3$ which must intersect for there to be a valid configuration (x, y) of the five-bar tail. Hence, after expansion of Eq. (32) for $i = 2$ and subtracting the corresponding expansion for $i = 3$ from it,

$$y = \frac{2(a_{x2} - a_{x3})x + \phi}{2(a_{y3} - a_{y2})} = \epsilon_1 x + \epsilon_0 \quad (33)$$

[1] Note, due to computational efficiency and kinematic constraints, an upper bound should also be placed in practice

where $\phi = {\rho_2}^2 - {\rho_3}^2 + {a_{x3}}^2 - {a_{x2}}^2 + {a_{y3}}^2 - {a_{y2}}^2$.

Substituting Eq. (33) into Eq. (32) for y and $i = 2$, a quadratic equation in x results

$$B_2 x^2 + B_1 x + B_0 = 0 \tag{34}$$

where $B_2 = {\epsilon_1}^2 + 1$, $B_1 = -2a_{x2} + 2\epsilon_1\epsilon_0 - 2a_{y2}\epsilon_1$ and $B_0 = {\epsilon_0}^2 - 2a_{y2}\epsilon_0 + {a_{x2}}^2 + {a_{y2}}^2 - {\rho_2}^2$. As such, x can be readily solved and the corresponding y determined.

With a feasible (x, y) determined for a viable set $(x_{c2}, y_{c2}, x_{c3}, y_{c3})$, the corresponding joint angles q_{ia} and q_{ib} can be found using the inverse geometric model (IGM). The IGM is formed by taking Eq. (30) and applying the steps of Eq. (26) and Eq. (28)-(29) to it. This yields a quadratic equation in u_{ia} with coefficients C_i from which q_{ia} can be determined

$$q_{ia} = 2\arctan\left(\frac{-C_1 \pm \sqrt{{C_1}^2 - 4C_0C_2}}{2C_2}\right) \tag{35}$$

i.e. for each configuration of the five bar linkage (x, y), there are two potential values of q_{ia}. These are termed the working modes of leg i.

With q_{ia} known, the associated values of the passive joints q_{ib} can be found, i.e. from Eq. (30)

$$q_{ib} = \arctan\left(\frac{y - l_{ia}s_{ia}}{x - l_{ia}c_{ia} - r_i}\right) - q_{ia} \tag{36}$$

Hence, the potential stationary points of the five-bar tail have been found. However, a further check should be made to eliminate any viable set in which the geometry of the configuration leads to intersection of limbs or that of singular configurations (particularly parallel singularities which theoretically yields an infinite force at the common end point).

REFERENCES

[1] Angeles, J., 2007, *Fundamentals of Robotic Mechanical Systems: Theory, Methods and Algorithms*, 3 ed. Springer.

[2] Abeywardena, S., and Chen, C., 2017, "Inverse dynamic modelling of a three-legged six-degree-of-freedom parallel mechanism," *Multibody System Dynamics,* **41**(1), pp. 1–24.